

# LA-UR-13-27078

Approved for public release; distribution is unlimited.

Title: Higher-Mode Applications of Fission Matrix Capability for MCNP

Author(s): Carney, Sean E.  
Brown, Forrest B.  
Kiedrowski, Brian C.  
Martin, William R.

Intended for: MCNP documentation  
Report  
Web

Issued: 2013-09-11



**Disclaimer:**

Los Alamos National Laboratory, an affirmative action/equal opportunity employer, is operated by the Los Alamos National Security, LLC for the National Nuclear Security Administration of the U.S. Department of Energy under contract DE-AC52-06NA25396. By approving this article, the publisher recognizes that the U.S. Government retains nonexclusive, royalty-free license to publish or reproduce the published form of this contribution, or to allow others to do so, for U.S. Government purposes. Los Alamos National Laboratory requests that the publisher identify this article as work performed under the auspices of the U.S. Department of Energy. Los Alamos National Laboratory strongly supports academic freedom and a researcher's right to publish; as an institution, however, the Laboratory does not endorse the viewpoint of a publication or guarantee its technical correctness.

# Higher-Mode Applications of Fission Matrix Capability for MCNP

Sean Carney<sup>1</sup>, Forrest Brown<sup>2</sup>, Brian Kiedrowski<sup>2</sup>, William Martin<sup>1</sup>

<sup>1</sup> *University of Michigan, 2355 Bonisteel Boulevard, Ann Arbor, MI 48109*

<sup>2</sup> *Los Alamos National Laboratory, P.O. Box 1663 MS A143, Los Alamos, NM 87545*

*seanec@umich.edu*

*August 2013*

## 1. INTRODUCTION

In this work, the fission matrix method [1][2], implemented into MCNP6 [3], is used to study criticality calculations and compute quantities of practical use. Physically, the fission matrix consists of spatial transition terms between two fission generations. With a sufficiently refined mesh (achieved here with a sparse storage scheme) these rates can be accurately tallied without knowledge of the correct fission distribution. The matrix can then be solved for K-eigenvalues and eigenvectors. The right and left eigenvectors correspond to forward and adjoint fission source modes, respectively.

Using higher source modes, the manner in which neutrons propagate in space through generations is represented with eigenmode expansions (section 3.1). Source convergence in criticality calculations is examined for a 2D Pressurized Water Reactor (PWR) problem in section 4.2. Three different initial guesses are used: a center point, corner point, and flat distribution. The cycle-wise sources are expanded into a sum of source modes, and details of convergence are discussed. Expansion coefficients over cycles for the first 30 modes are shown, and their decay rates are found to agree closely with expected values found from the eigenvalue spectrum.

Using forward source modes from the fission matrix, the first 30 forward flux modes are calculated for the 2D PWR problem by running fixed-source calculations. Flux modes are shown in section 4.1 for both the thermal and above-thermal neutron energy range. For these results, high relative variance is found to be localized to inflection lines.

Also of interest are higher modes of adjoint-weighted flux; these are not easily found while maintaining the accurate spatial and energy representation of Monte Carlo. Here, a new method of calculating these functions using higher-mode information from the fission matrix is examined. This extends previous work to perform fundamental-mode adjoint-weighting, which uses the concept of iterated fission probability to weight flux tallies [4].

To perform higher-mode adjoint weighting, a technique called fission kernel deflation is introduced, in which criticality calculations are altered to converge to higher source modes. It is then argued in sections 3.4-6, through the eigenvalue expansion of the Green's function, that fission kernel deflation combined with iterated fission proba-

bility weighting results in higher-mode adjoint weighting.

A 3-group slab problem is ran to verify the stable convergence of the kernel deflation technique. Agreement of the first six fission source modes with expectation is shown in section 4.4. Higher-mode adjoint weighting is then applied to this problem, and results are benchmarked with a discrete ordinates code written in Matlab. In section 4.5, plots of the first four adjoint-weighted flux modes show reasonable agreement with discrete ordinates, though an increasing bias for higher mode number is seen.

Additionally, two applications of higher-mode adjoint weighting, second-order perturbation theory and quasi-static transient calculations, are discussed (sections 3.8-9) in the context of the proposed weighting scheme. Included is a derivation of the second-order perturbation theory equations.

## 2. MOTIVATION

Nuclear engineering design work involves fine-tuning parameters, in order to search a design space. Direct, brute-force parameter studies, which involve many independent calculations of varying input, is time-consuming in the context of man-power. An additional burden arises from Monte Carlo calculations, as calculating a precise and small difference between two stochastic results is time-consuming. Perturbation theory allows for a design space to be searched more efficiently, in the sense of both issues. This methodology involves the pre-computation of sensitivities, which allows for extrapolations from a base case.

Second order perturbation theory increases the applicable range of extrapolation into design space. Lacking from the first-order formulation, the second-order formulation approximates changes in the flux shape due to a perturbation. This requires higher-mode flux information, both forward and adjoint. The fission matrix method allows for calculating higher source modes; Monte Carlo cannot easily calculate higher-mode information without this method. A potential application of the fission matrix method is extending perturbation theory to second-order.

Similar to this extension is the quasi-static method, which approximates time-dependent behavior by calculating the time-dependency of higher modes. Reliable approximations of time-dependent behavior are very useful, due to the high cost of rigorous Monte Carlo transient cal-

culations.

These theories apply both to forward and inverse neutron transport problems. Common forward problems of applicability here are: Boiling Water Reactor (BWR) power oscillations, xenon oscillations, control rod movement and interaction, and long-term burnup effects. Inverse problems consist primarily of the estimation of system parameters using radiation detector responses.

There are also applications of eigenmode expansions, discussed in sections 3.1 and 4.2. With precise convergence knowledge gained from modal information, the iterated fission probability method of adjoint-weighting, discussed in section 3.3, can be better understood. It is possible to quantify the number of necessary latent generations, dependent upon space, necessary for these calculations. Another area of interest is the normality of eigenmode expansion coefficients, examined by Toth, et al. [5]. This subject is also relevant to the concern of inter-cycle correlation, and its effect on variance under-estimation [6]. The use of higher eigenvalues was found to improve variance estimates on a 1-group slab problem in previous work [7].

An additional application of eigenmode expansion is the representation of a perturbed system's fundamental mode with eigenmodes of an unperturbed system. This can indicate (in neutron generations), the time until the perturbed system settles to steady state, and the spatial manner in which it does so. This also may have relevance to the degree of coupling needed between neutronics and thermal-hydraulics calculations, if such a method is used. Lastly, it indicates the ability of a limited number of fission source modes of the unperturbed system to represent the fundamental mode of the perturbed system.

### 3. THEORY

#### 3.1. Modal expansion of fission source

In a criticality calculation, expanding the fission bank distribution of cycle  $c$ ,  $f^c(\vec{r})$ , with the fission source eigenvectors  $S_n(\vec{r})$  can give insight into the power iteration process. Yamamoto, et al. [8] have shown this by using eigenmodes calculated with the method of characteristics. The modal expansion coefficients  $a_n^c$ —found using biorthogonality [Eqs. (1)]—indicate the relative importance of different eigenmodes. Typically convergence is only characterized by the dominance ratio,  $K_1/K_0$ , but this expansion,

$$f^c(\vec{r}) = \sum_{n=0}^{\hat{N}} a_n^c S_n(\vec{r}), \quad (1a)$$

$$a_n^c = \frac{\langle f^c(\vec{r}) S_n^\dagger(\vec{r}) \rangle}{\langle S_n(\vec{r}) S_n^\dagger(\vec{r}) \rangle}, \quad (1b)$$

gives more information.  $\hat{N}$  is a maximum mode number of interest, less than the total number of modes. To calculate  $a_n^c$ , left and right eigenvectors of a tallied fission matrix are calculated. These are then used for the cycle-wise calculation of Eq. (1b) on the same problem with varying initial source guess. Different guesses will excite different modes.

Recalling the proof of power iteration convergence rate, which assumes linearly independent eigenvectors (the case here), the decay rate of mode  $n > 0$  is given by  $K_n/K_0$ . Similar rates for the expansion coefficients here would be expected.

#### 3.2. Calculation of forward flux modes

The right eigenvectors of the fission matrix,

$$S_n(\vec{r}) = \iint dE' d\hat{\Omega}' \nu \Sigma_F(\vec{r}, E') \Psi_n(\vec{r}, E', \hat{\Omega}'), \quad (2)$$

can be used to calculate forward flux modes. This requires running a fixed-source calculation on  $S_n(\vec{r})$ ,

$$\Psi_n(\vec{r}, E, \hat{\Omega}) = \frac{1}{K_n} \mathbf{M}^{-1} \cdot \frac{\chi(\vec{r}, E)}{4\pi} S_n(\vec{r}). \quad (3)$$

As both flux and fission source modes vary with sign for  $n > 0$ , a flag is needed to mark the particle weight's sign. Consequently, handling both positive and negative scores is necessary in tally routines. The current implementation involves repeated calls to MCNP6 with fission sources of increasing mode number, and a track-length flux tally on a Cartesian, energy-binned mesh. The NONU card is used to treat fission as absorption—this is necessary from the definition of the net-loss operator. Source points are sampled in an analog manner (using an alias table) from the loaded fission source mode, and location is re-sampled until fissionable material is found. An equivalent, and possibly more efficient method, is to hold all desired modal information in each particle history. This entails sampling source points uniformly throughout the problem's fissionable regions, and attaching a vector of weights to each source particle. Each weight here corresponds to the different fission source mode values at the relevant location. The different weights are then treated as usual for a random walk.

A concern here is that for greater positive/negative oscillation in the source as mode number rises, there will be more score cancellation in tallies. This may lead to larger tally variances than is manageable. This issue is examined in section 4.1.

#### 3.3. Calculation of adjoint flux modes

It has been proven [1] that for a fine enough mesh, the left-eigenvectors of the fission matrix are equivalent to the

adjoint fission source modes,

$$S_n^\dagger(\vec{r}) = \int \int dE' d\hat{\Omega}' \frac{\chi(\vec{r}, E')}{4\pi} \Psi_n^\dagger(\vec{r}, E', \hat{\Omega}'). \quad (4)$$

Analogous to Eq. (3), the inverse of the adjoint net loss operator could theoretically be applied to  $\nu_{\Sigma_F}(\vec{r}, E) S_n^\dagger(\vec{r})$  to obtain adjoint flux modes. This is highly impractical to implement, though, due primarily to the difficulty of transposing the scattering operator. A tally of scattering matrices and multigroup treatment could allow for easy transposing, but this is a significant complication, and reduces the fidelity of the Monte Carlo calculation.

Previously, a method has been developed and implemented in MCNP to perform continuous-energy adjoint weighting of tallies [4]. This method uses the iterated fission probability interpretation of adjoint flux. In broad terms, adjoint weighting of a tally is proportional to the near-asymptotic neutron population resulting from the tally contributing neutron. This involves: an original generation where tallies and their respective neutron "progenitor" identifiers are stored, a number of latent generations in which progenitors yield subsequent progeny, and an asymptotic generation where the original tallies are weighted by population. Below is an attempted extension of this method—to weighting by higher-mode adjoint functions.

### 3.4. Deflation of the fission kernel

The iterated fission probability interpretation of adjoint flux can be summarized with the following statement of proportionality,

$$\begin{aligned} \Psi^\dagger(\vec{r}_0, E_0, \hat{\Omega}_0) &= c \times \langle F(\vec{r}' \rightarrow \vec{r})^L. \\ \iint dE' d\hat{\Omega}' G(\vec{r}_0, E_0, \hat{\Omega}_0 \rightarrow \vec{r}', E', \hat{\Omega}') \nu_{\Sigma_F}(\vec{r}', E') \rangle_{\vec{r}}, \end{aligned} \quad (5)$$

where  $L$  is the number of latent generations used,  $F(\vec{r}' \rightarrow \vec{r})$  is the fission kernel, and  $c$  is an arbitrary constant. In words: the adjoint flux at a point is proportional to  $L+1$  repeated fission generations applied to a point source at  $(\vec{r}_0, E_0, \hat{\Omega}_0)$ . As a side note, the assumption of asymptotic population after  $L$  generations is equivalent to

$$\begin{aligned} &F(\vec{r}' \rightarrow \vec{r})^L \\ &\cdot \iint dE' d\hat{\Omega}' G(\vec{r}_0, E_0, \hat{\Omega}_0 \rightarrow \vec{r}', E', \hat{\Omega}') \nu_{\Sigma_F}(\vec{r}', E') \\ &\approx c S_0(\vec{r}), \end{aligned} \quad (6)$$

where  $c$  is a scaling constant and  $S_0(\vec{r})$  is the fundamental fission source mode.

The above representations of iterated fission probability suggest an extension—of weighting by higher modes using the concept of matrix deflation. Matrix deflation eliminates the effect of eigenvectors (those which the matrix is deflated by). With Hotelling deflation of degree  $n - 1$ ,

$$F_n = F - \sum_{n'=0}^{n-1} K_{n'} \frac{S_{n'} S_{n'}^\dagger}{\langle S_{n'}^\dagger S_{n'} \rangle}, \quad (7)$$

repeated application of the deflated matrix results in convergence to mode  $n$ . With the forward/adjoint fission source modes and eigenvalues found from the diagonalization of the fission matrix, it is possible to perform deflation with regards to the fission kernel,

$$\begin{aligned} F_n(\vec{r}_0 \rightarrow \vec{r}) &= F_0(\vec{r}_0 \rightarrow \vec{r}) - \sum_{n'=0}^{n-1} K_{n'} \frac{S_{n'}(\vec{r}) S_{n'}^\dagger(\vec{r}_0)}{\langle S_{n'}^\dagger(\vec{r}') S_{n'}(\vec{r}') \rangle} \\ &= \iiint dE d\hat{\Omega} dE_0 d\hat{\Omega}_0 \nu_{\Sigma_F}(\vec{r}, E) \left[ G(\vec{r}_0, E_0, \hat{\Omega}_0 \rightarrow \vec{r}, E, \hat{\Omega}) \right. \\ &\quad \left. - \sum_{n'=0}^{n-1} K_{n'} \frac{\Psi_{n'}(\vec{r}, E, \hat{\Omega}) \Psi_{n'}^\dagger(\vec{r}_0, E_0, \hat{\Omega}_0)}{\langle S_{n'}^\dagger(\vec{r}') S_{n'}(\vec{r}') \rangle} \right] \frac{\chi(\vec{r}_0, E_0)}{4\pi}. \end{aligned} \quad (8)$$

Returning now to the subject of iterated fission probability, it seems likely that by eliminating the effects of leading modes and applying the iterated fission probability method, weighting by higher adjoint modes is possible.

### 3.5. Relationship between Green's function and flux modes

This proof, similar to one found in Duderstadt & Hamilton [9], will show the relationship between flux modes and the Green's function, thus giving context for the deflation method discussed in section 3.4. This begins with the k-eigenvalue form of the transport equation,

$$\mathbf{M} \cdot \Psi(\vec{r}, E, \hat{\Omega}) = \frac{1}{K} \frac{\chi(\vec{r}, E)}{4\pi} S(\vec{r}), \quad (9)$$

and expanding the fission source and angular flux modes,

$$\Psi(\vec{r}, E, \hat{\Omega}) = \sum_{n=0}^{\infty} c_n \Psi_n(\vec{r}, E, \hat{\Omega}), \quad (10)$$

$$S(\vec{r}) = \sum_{n=0}^{\infty} s_n S_n(\vec{r}). \quad (11)$$

Eq. (10) is not true in general, as discussed in [10]. The implications of this may be important in the context of kernel deflation as a whole. Now, solving for the source expansion coefficients is done using biorthogonality,

$$s_n = \frac{\langle \Psi_n^\dagger(\vec{r}, E, \hat{\Omega}), \frac{\chi(\vec{r}, E)}{4\pi} S(\vec{r}) \rangle}{\langle \Psi_n^\dagger(\vec{r}, E, \hat{\Omega}), \frac{\chi(\vec{r}, E)}{4\pi} S_n(\vec{r}) \rangle}. \quad (12)$$

This result, along with the flux expansion, is inserted into transport equation,

$$\mathbf{M} \cdot \sum_{n=0}^{\infty} c_n \Psi_n(\vec{r}, E, \hat{\Omega}) = \frac{1}{K} \frac{\chi(\vec{r}, E)}{4\pi} \sum_{n=0}^{\infty} s_n S_n(\vec{r}). \quad (13)$$

The net loss operator is then applied to the flux modes, and the transport equation for higher modes is used,

$$\sum_{n=0}^{\infty} c_n \frac{1}{K_n} \frac{\chi(\vec{r}, E)}{4\pi} S_n(\vec{r}) = \frac{1}{K} \frac{\chi(\vec{r}, E)}{4\pi} \sum_{n=0}^{\infty} s_n S_n(\vec{r}). \quad (14)$$

Again using biorthogonality, the following relation between the two expansion coefficients is found,

$$c_n = \frac{K_n}{K_0} s_n. \quad (15)$$

Plugging this relation into the flux expansion gives

$$\begin{aligned} \Psi(\vec{r}, E, \hat{\Omega}) = \\ \frac{1}{K_0} \sum_{n=0}^{\infty} K_n \frac{\langle \Psi_n^\dagger(\vec{r}', E', \hat{\Omega}'), \frac{\chi(\vec{r}', E')}{4\pi} S(\vec{r}') \rangle}{\langle \Psi_n^\dagger(\vec{r}', E', \hat{\Omega}'), \frac{\chi(\vec{r}', E')}{4\pi} S_n(\vec{r}') \rangle} \Psi_n(\vec{r}, E, \hat{\Omega}). \end{aligned} \quad (16)$$

Recalling the integral transport equation,

$$\begin{aligned} \Psi(\vec{r}, E, \hat{\Omega}) = \frac{1}{K_0} \iiint d\vec{r}_0 dE_0 d\hat{\Omega} \frac{\chi(\vec{r}_0, E_0)}{4\pi} \\ S(\vec{r}_0) G(\vec{r}_0, E_0, \hat{\Omega}_0 \rightarrow \vec{r}, E, \hat{\Omega}), \end{aligned} \quad (17)$$

and comparing to Eq. (16) indicates

$$\begin{aligned} G(\vec{r}_0, E_0, \hat{\Omega}_0 \rightarrow \vec{r}, E, \hat{\Omega}) = \\ \sum_{n=0}^{\infty} K_n \frac{\Psi_n(\vec{r}, E, \hat{\Omega}) \Psi_n^\dagger(\vec{r}_0, E_0, \hat{\Omega}_0)}{\langle S_n^\dagger(\vec{r}'), S_n(\vec{r}') \rangle}. \end{aligned} \quad (18)$$

With this expression of the Green's function, Eq. (8) is given more substantial meaning. In a similar manner, the following eigenvalue expansion of the adjoint Green's function can be derived:

$$\begin{aligned} G^\dagger(\vec{r}_0, E_0, \hat{\Omega}_0 \rightarrow \vec{r}, E, \hat{\Omega}) = \\ \sum_{n=0}^{\infty} K_n \frac{\Psi_n^\dagger(\vec{r}, E, \hat{\Omega}) \Psi_n(\vec{r}_0, E_0, \hat{\Omega}_0)}{\langle S_n^\dagger(\vec{r}'), S_n(\vec{r}') \rangle}. \end{aligned} \quad (19)$$

### 3.6. Attempted Proof of Higher-Mode Adjoint Weighting

Assuming the Green's function eigenvalue expansion [Eq. (18)], a proof of the main principle of iterated fission probability weighting [Eq. (5)] is attempted. This is then extended to the deflated kernel, to justify the higher-mode adjoint weighting method proposed.

First, an expression for  $F(\vec{r}' \rightarrow \vec{r})^L$  is found using the Green's function eigenvalue expansion. Examining the case of  $L = 2$ ,

$$\begin{aligned} F(\vec{r}_0 \rightarrow \vec{r})^2 = F(\vec{r}' \rightarrow \vec{r}) F(\vec{r}_0 \rightarrow \vec{r}') = \\ \left( \sum_{n=0}^{\infty} K_n \frac{S_n(\vec{r}) S_n^\dagger(\vec{r}')}{\langle S_n^\dagger(\vec{r}'') S_n(\vec{r}'') \rangle} \right) \\ \times \left( \sum_{m=0}^{\infty} K_m \frac{S_m(\vec{r}') S_m^\dagger(\vec{r}_0)}{\langle S_m^\dagger(\vec{r}'') S_m(\vec{r}'') \rangle} \right), \end{aligned} \quad (20)$$

this equality involved using the expansion of Eq. (18) and evaluating the integrals necessary to get to the forward/adjoint fission source mode terms. In the context of the fission matrix, Eq. (20) resembles matrix diagonalization on a infinitely-fine mesh. Next, these two infinite series of outer products are multiplied with each other; the  $n \neq m$  terms cancel due to biorthogonality,

$$\begin{aligned} F(\vec{r}_0 \rightarrow \vec{r})^2 = \\ \sum_{n=0}^{\infty} K_n^2 \frac{S_n(\vec{r}) \langle S_n^\dagger(\vec{r}'') S_n(\vec{r}'') \rangle S_n^\dagger(\vec{r}')}{\langle S_n^\dagger(\vec{r}'') S_n(\vec{r}'') \rangle^2} = \\ \sum_{n=0}^{\infty} K_n^2 \frac{S_n(\vec{r}) S_n^\dagger(\vec{r}')}{\langle S_n^\dagger(\vec{r}'') S_n(\vec{r}'') \rangle}. \end{aligned} \quad (21)$$

By extension, the expression for arbitrary  $L$  is

$$F(\vec{r}_0 \rightarrow \vec{r})^L = \sum_{n=0}^{\infty} K_n^L \frac{S_n(\vec{r}) S_n^\dagger(\vec{r}_0)}{\langle S_n^\dagger(\vec{r}'') S_n(\vec{r}'') \rangle}. \quad (22)$$

Now, insert this expression into the right side of Eq. (5) and expand the Green's function applied in the original generation,

$$\begin{aligned}
& F(\vec{r}' \rightarrow \vec{r})^L. \\
& \iint dE' d\hat{\Omega}' G(\vec{r}_0, E_0, \hat{\Omega}_0 \rightarrow \vec{r}', E', \hat{\Omega}') \nu \Sigma_F(\vec{r}', E') = \\
& \left[ \sum_{n=0}^{\infty} K_n^L \frac{S_n(\vec{r}) S_n^\dagger(\vec{r}')}{\langle S_n^\dagger(\vec{r}'') S_n(\vec{r}'') \rangle} \right] \\
& \quad \times \left[ \iint dE' d\hat{\Omega}' \right. \\
& \left. \sum_{m=0}^{\infty} K_m \frac{\Psi_m(\vec{r}', E', \hat{\Omega}') \Psi_m^\dagger(\vec{r}_0, E_0, \hat{\Omega}_0) \nu \Sigma_F(\vec{r}', E')}{\langle S_m^\dagger(\vec{r}'') S_m(\vec{r}'') \rangle} \right]. \quad (23)
\end{aligned}$$

Evaluating the double integral on the right yields forward source mode terms. Multiply the two infinite series and use biorthogonality,

$$\begin{aligned}
& F(\vec{r}' \rightarrow \vec{r})^L \cdot [\dots] = \\
& \left[ \sum_{n=0}^{\infty} K_n^L \frac{S_n(\vec{r}) S_n^\dagger(\vec{r}')}{\langle S_n^\dagger(\vec{r}'') S_n(\vec{r}'') \rangle} \right] \\
& \quad \times \left[ \sum_{m=0}^{\infty} K_m \frac{S_m(\vec{r}') \Psi_m^\dagger(\vec{r}_0, E_0, \hat{\Omega}_0)}{\langle S_m^\dagger(\vec{r}'') S_m(\vec{r}'') \rangle} \right] = \\
& \quad \sum_{n=0}^{\infty} K_n^{L+1} \frac{S_n(\vec{r}) \Psi_n^\dagger(\vec{r}_0, E_0, \hat{\Omega}_0)}{\langle S_n^\dagger(\vec{r}'') S_n(\vec{r}'') \rangle}. \quad (24)
\end{aligned}$$

Lastly, account for the renormalization that occurs after every cycle of the power iteration process, i.e. divide by  $K_0^{L+1}$ ,

$$\begin{aligned}
& F(\vec{r}' \rightarrow \vec{r})^L \cdot [\dots] = \\
& \frac{S_0(\vec{r}) \Psi_0^\dagger(\vec{r}_0, E_0, \hat{\Omega}_0)}{\langle S_0^\dagger(\vec{r}'') S_0(\vec{r}'') \rangle} + \\
& \left( \frac{K_1}{K_0} \right)^{L+1} \frac{S_1(\vec{r}) \Psi_1^\dagger(\vec{r}_0, E_0, \hat{\Omega}_0)}{\langle S_1^\dagger(\vec{r}'') S_1(\vec{r}'') \rangle} + \\
& \left( \frac{K_2}{K_0} \right)^{L+1} \frac{S_2(\vec{r}) \Psi_2^\dagger(\vec{r}_0, E_0, \hat{\Omega}_0)}{\langle S_2^\dagger(\vec{r}'') S_2(\vec{r}'') \rangle} + \dots \quad (25)
\end{aligned}$$

Assuming the number of latent generations has been sufficient, i.e. higher modes have been powered out, only the mode-0 term remains. The final rearranged result is then

$$\begin{aligned}
& \Psi_0^\dagger(\vec{r}_0, E_0, \hat{\Omega}_0) = \\
& \frac{\langle S_0^\dagger(\vec{r}'') S_0(\vec{r}'') \rangle}{S_0(\vec{r})} F(\vec{r}' \rightarrow \vec{r})^L \cdot [\dots] = \\
& \langle S_0^\dagger(\vec{r}'') S_0(\vec{r}'') \rangle \cdot c \quad (26)
\end{aligned}$$

The assumption of asymptotic population, Eq. (6), has been used; the constant  $c$  represents the asymptotic population size, which can validly be tallied over the entire problem for the greatest sampling efficiency. This equality, which has been arrived at through eigenvalue expansion of the Green's function, states the fundamental principle of iterated fission probability, Eq. (5). Now, this is examined in the context of the deflated kernel.

The deflation process, which uses source eigenvectors from the fission matrix on a spatial mesh, approximates the following equality:

$$F_n(\vec{r}_0 \rightarrow \vec{r})^L = \sum_{n'=n}^{\infty} K_{n'}^L \frac{S_{n'}(\vec{r}) S_{n'}^\dagger(\vec{r}_0)}{\langle S_{n'}^\dagger(\vec{r}'') S_{n'}(\vec{r}'') \rangle}. \quad (27)$$

Using the same argument as Eqs. (23) and (24), but with the deflated kernel, the following series is found:

$$\begin{aligned}
& F_n(\vec{r}' \rightarrow \vec{r})^L \cdot [\dots] = \\
& \frac{S_n(\vec{r}) \Psi_n^\dagger(\vec{r}_0, E_0, \hat{\Omega}_0)}{\langle S_n^\dagger(\vec{r}'') S_n(\vec{r}'') \rangle} + \\
& \left( \frac{K_{n+1}}{K_n} \right)^{L+1} \frac{S_{n+1}(\vec{r}) \Psi_{n+1}^\dagger(\vec{r}_0, E_0, \hat{\Omega}_0)}{\langle S_{n+1}^\dagger(\vec{r}'') S_{n+1}(\vec{r}'') \rangle} + \\
& \left( \frac{K_{n+2}}{K_n} \right)^{L+1} \frac{S_{n+2}(\vec{r}) \Psi_{n+2}^\dagger(\vec{r}_0, E_0, \hat{\Omega}_0)}{\langle S_{n+2}^\dagger(\vec{r}'') S_{n+2}(\vec{r}'') \rangle} + \dots \quad (28)
\end{aligned}$$

Powering higher modes out gives an expression for the principle of iterated fission probability on a deflated kernel,

$$\begin{aligned}
& \Psi_n^\dagger(\vec{r}_0, E_0, \hat{\Omega}_0) = \\
& \frac{\langle S_n^\dagger(\vec{r}'') S_n(\vec{r}'') \rangle}{S_n(\vec{r})} F_n(\vec{r}' \rightarrow \vec{r})^L \cdot [\dots] = \\
& \langle S_n^\dagger(\vec{r}'') S_n(\vec{r}'') \rangle \cdot c_n, \quad (29)
\end{aligned}$$

where another assumption of asymptotic population has been made—the size given by  $c_n$ . Note  $c_n$  can now be positive or negative. This means that the sign of the asymptotic distribution given by repeated application of  $F_n$  to the origin point  $(\vec{r}_0, E_0, \hat{\Omega}_0)$  can be opposite in sign to the reference distribution  $S_n(\vec{r})$ . For this argument the weight of the origin point has been defined as positive and unity (generalizing to include an extra term for the sign-varying weight of the origin point in the fission kernel would give the same conclusion). Recalling the discussion of power iteration and eigenmode expansion, convergence to either  $\pm S_n(\vec{r})$  is possible, depending on which sign of the mode is excited initially. The sign of the mode that is excited is thus given by the sign of the adjoint flux mode at that point.

The magnitude of  $c_n$  is found, as before, by tallying the size of the asymptotic population. The sign of  $c_n$  must also

be calculated now, by finding the sign of the asymptotic distribution relative to the reference source  $S_n(\vec{r})$ . The simplest way to do this (the source may not be completely converged, so the sign estimation cannot always be perfect) seems to be to compute the inner product,

$$sign(c_n) = sign(\langle S_n^\dagger(\vec{r}), F_n(\vec{r}' \rightarrow \vec{r})^L \cdot [\dots] \rangle), \quad (30)$$

which considers all of the asymptotic progeny, and weights by importance of location. This requires extra work and memory in every asymptotic generation-related progeny must be gathered together to compute the inner products.

As will be shown, the current adjoint weighting method shows bias; peaks are underestimated and critical points are overestimated. This could be primarily due to two effects of critical points: near division by zero (implicitly) during weighting in the asymptotic generation, and sign-variation of the fission source across multiple original generations. Special treatment near critical points may be required for more accurate higher-mode adjoint weighting.

There is presently a difference in the asymptotic population estimation for higher-modes, as compared to mode-0. Mode-0 weighting effectively computes the expected-value of population, by tallying the fission-production rate with a track-length estimator. This fission-production rate is not relevant to higher modes. Presently, higher-mode population is estimated in an analog manner, by counting fission sites. An expected value approach could be implemented, though, with a track-length tally on the same mesh as the deflation vectors.

### 3.7. Applying kernel deflation

The method of deflation used here involves alteration of inter-cycle fission banks on a finite spatial mesh. An exact deflation would require directly altering the random walk to directly yield higher modes; here the application of the deflated kernel on a cycle-wise fission source  $S^c(\vec{r}_0)$  is decomposed,

$$F_n(\vec{r}_0 \rightarrow \vec{r}) \cdot S^c(\vec{r}_0) = F_0(\vec{r}_0 \rightarrow \vec{r})S^c(\vec{r}_0) - \sum_{n'=0}^{n-1} K_{n'} \frac{\langle S_{n'}^\dagger(\vec{r}_0)S^c(\vec{r}_0) \rangle}{\langle S_{n'}^\dagger(\vec{r}')S_{n'}(\vec{r}') \rangle} S_{n'}(\vec{r}). \quad (31)$$

The first term on the right side of Eq. (31) represents the normal transport of a fission generation. The numerator of the second term represents an inner product of the cycle-wise source with an adjoint fission source mode; this gives the degree to which the present source is exciting modes that should be eliminated. The first term is spatially discretized, in order to subtract the already-discretized second term (scaled by inner products saved from before the last

cycle). The vector resulting from the subtraction of the two terms is then replicated in inter-cycle fission banks. To ensure stability, the first term on the right side must be scaled by a ratio to ensure its growth in magnitude conforms to the growth of the second term. Uncorrected, the first term's growth is stochastic, whereas the second term's growth is deterministic.

The way in which a spatial distribution is replicated in the fission bank is now discussed, as the previously used method was found to be unstable when inflection points are present. The method used in past fission matrix studies consisted of:

1. Spatially bin current fission bank on identical mesh to desired source, to get a current spatial distribution,
2. Using every current source point's location in the mesh, store ratio of desired spatial distribution value to current value,
3. Use these ratios, stored for every site, to duplicate or delete sites and best match desired distribution.

This works well for normal cases, but not here, where higher modes containing sign changes are to be replicated. Storing a ratio of distributions does not work well, because of the possible division by small values. Instead, a less efficient method is used,  $O(N_{mesh}N_{bank})$  as opposed to  $O(N_{bank})$ , where  $N_{mesh}$  is the number of mesh cells in the desired distribution and  $N_{bank}$  is the number of points in the fission bank. This algorithm, which avoids the use of ratios, is as follows:

1. Spatially bin fission bank on identical mesh to desired source, to get a current spatial distribution,
2. Zero out values in desired distribution where no points are present,
3. Sample  $N_{bank}$  mesh cell indices from desired distribution,
4. Build a sorting vector to index into the fission bank by increasing mesh index,
5. Sample points from sorted fission bank—the number of points for each mesh cell is given by the number of repeated indices from step #3.

With this slower method, issues near inflection points are avoided.

### 3.8. Second-order perturbation theory

Below is an outline of second-order perturbation theory, which involves expansion of the flux perturbation present in second-order terms into a sum of higher flux modes. Similar results are found in Ref. [11], and relevant

theory is discussed in Ref. [10]. Use of the additional spatial information should account for the effect of global flux changes on the fundamental eigenvalue. In Ref. [11], control rod interaction effects are studied with higher modes; calculating interactions scales factorially with the number of control rods, thus a spatial perturbation theory is used.

Starting by perturbing a base case,

$$L_0\phi_0 = \lambda_0 M_0\phi_0, \quad (32)$$

$$(L_0 + \delta L)(\phi_0 + \delta\phi) = (\lambda_0 + \delta\lambda)(M_0 + \delta M)(\phi_0 + \delta\phi), \quad (33)$$

and expanding the flux perturbation term with the unperturbed flux modes,

$$\delta\phi = \sum_{n=1}^{\hat{N}} a_n \Psi_n, \quad (34)$$

and removing all second and third-order terms gives

$$\delta L\phi_0 + L_0 \sum_{n=1}^{\hat{N}} a_n \Psi_n = \lambda_0 M_0 \sum_{n=1}^{\hat{N}} a_n \Psi_n + \lambda_0 \delta M\phi_0 + \delta\lambda M_0\phi_0. \quad (35)$$

Left multiplying by the adjoint flux, taking the inner product, and using orthogonality ( $\langle \Psi_m^\dagger, M_0 \Psi_n \rangle = \delta_{nm} \langle \Psi_n^\dagger, M_0 \Psi_n \rangle$ ),

$$a_n = \frac{\langle \Psi_n^\dagger, (\delta L - \lambda_0 \delta M)\phi_0 \rangle + \delta\lambda \langle \Psi_n^\dagger, M_0 \phi_0 \rangle}{(\lambda_0 - \lambda_n) \langle \Psi_n^\dagger, M_0 \Psi_n \rangle}. \quad (36)$$

The left term in the numerator of Eq. (36) is computed with perturbed calculations in original generations, followed by higher-mode adjoint weighting. As an aside, the need for adjoint weighting of the other terms can be eschewed by calculating the equivalent inner product,

$$\begin{aligned} \langle \Psi_n^\dagger, M_0 \Psi_n \rangle &= \langle \Psi, M_0^\dagger \Psi^\dagger \rangle \\ &= \iiint d\vec{r} dE d\hat{\Omega} \Psi_n(\vec{r}, E, \hat{\Omega}) \nu \Sigma_F(\vec{r}, E) S_n^\dagger(\vec{r}). \end{aligned} \quad (37)$$

$\delta\lambda$  in Eq. (36) is approximated with the standard first-order approximation. Now, expanding Eq. (33) and neglect only third-order terms yields

$$\begin{aligned} \delta L\phi_0 + L_0\delta\phi + \delta L\delta\phi \\ &= \lambda_0 M_0\phi_0 + \lambda_0 \delta M\phi_0 + \lambda \delta M\delta\phi \\ &\quad + \delta\lambda M_0\phi_0 + \delta\lambda M_0\delta\phi + \delta\lambda \delta M\phi_0. \end{aligned} \quad (38)$$

Weighting by the fundamental adjoint, taking the inner product, and using the defining property of adjoint operators,

$$\langle \Psi_0^\dagger, (L - \lambda_0 M)\delta\phi \rangle = \langle \delta\phi, (L^\dagger - \lambda_0 M^\dagger)\Psi_0^\dagger \rangle = 0, \quad (39)$$

and solving for  $\delta\lambda$  yields,

$$\begin{aligned} \delta\lambda &= \frac{\langle \Psi_0^\dagger, (\delta L - \lambda_0 \delta M)(\phi_0 + \delta\phi) \rangle}{\langle \Psi_0^\dagger, (M_0 + \delta M)\phi_0 \rangle + \langle \Psi_0^\dagger, M_0 \delta\phi_0 \rangle} \\ &= \frac{\langle \Psi_0^\dagger, (\delta L - \lambda_0 \delta M)\phi_0 \rangle + \sum_{n'=1}^{\hat{N}} a_{n'} \langle \Psi_0^\dagger, (\delta L - \lambda_0 \delta M)\Psi_{n'} \rangle}{\langle \Psi_0^\dagger, (M_0 + \delta M)\phi_0 \rangle + \sum_{n'=1}^{\hat{N}} a_{n'} \langle \Psi_0^\dagger, M_0 \Psi_{n'} \rangle}. \end{aligned} \quad (40)$$

The right term in the numerator entails running fixed-source calculations with higher modes in the original generations, and then performing mode-0 adjoint weighting.

### 3.9. Quasi-Static Modal Expansion Method

Starting from the time-dependent transport equation, flux can be expanded into products of unperturbed eigenmodes and time-dependent expansion coefficients. Using adjoint weighting of varying mode number, a system of first-order differential equations in time can be formulated and solved for the expansion coefficients. With these, transients and reactor stability can be studied. Refs. [12],[13] derive the relevant equations, and apply them with diffusion theory. Using diffusion theory, modes are periodically updated to account for the time-dependence of multigroup cross sections. By using Monte Carlo and a continuous energy treatment, this updating shouldn't be necessary.

Similar calculations can be done by expanding the steady state fission source distribution of a perturbed state as the sum of source modes of an unperturbed state. Relevant ratios of eigenvalues can be used to represent a transient in neutron generation-time. With the quasi-static system of equations, though, transients are represented in physical time. Delayed neutrons are explicitly accounted for, and unique kinetics parameters for each eigenmode, better model transient behavior.

In the quasi-static equations, a near-instantaneous perturbation could be represented in the perturbed operators ( $\delta L, \delta M$ ) with a Heaviside step function in time. Other transient phenomena, such as Xenon-induced power oscillations or BWR instabilities, could be represented with a frequency term in the perturbed operators.

### 3.10. Adjoint-weighted flux tallies

Before the calculation of higher adjoint flux modes, it was necessary to add a subroutine into MCNP that allowed for the calculation of adjoint-weighted flux,  $\langle \Psi^\dagger, \Psi \rangle_r$ , where  $r$  is a phase-space region in space and energy. While this calculation has been done in Ref. [4], it has not been implemented into the current version of MCNP6. To do this, two modules used for k-sensitivity calculations were

taken ('ksen\_xs\_mod.F90' and 'ksen\_interface\_mod.F90') as templates to write similar, yet simplified, modules ('kadj\_wgting\_mod.F90' and 'kadj\_wgting\_mod.F90'). In the future, a forward flux multiplier akin to the tally multiplier (FM) card will be added to these modules.

## 4. RESULTS

### 4.1. Forward flux

To test the forward flux calculations, a fission matrix was generated from a 2D PWR problem ( $50 \times 50 \times 1$  mesh; 500 cycles, initial 2 skipped; 500k batch size), and fixed-source calculations (500k histories) were ran for 30 modes. The same problem was examined in Refs. [2] and [7]. Figures 1 and 2 give flux results, and Figs. 3 and 4 show relative uncertainties. Times for these calculations were about a minute on 8 threads, for each mode. Group 1 flux modes are very similar to the fission source modes, and the most notable feature of the group 2 flux modes are the new peaks in the peripheral water moderator. The relative uncertainty plots give a reassuring result—the high relative uncertainties are localized near the inflection lines. Uncertainties are manageable where the functions are significantly nonzero, notwithstanding the cancellation of tallies.

### 4.2. Expansion coefficients

For the 2D PWR problem, cycle-wise eigenmode expansion coefficients as given by Eq. (1b) were calculated. Three initial guesses were chosen: a point in the center (Fig. 5), a point in the corner (Fig. 6), and uniform throughout the problem (Fig. 9). In these plots, important modes are labeled: the center guess excites radially-symmetric modes that have peaks in the center, the corner guess excites asymmetric modes that have peaks in the relevant corner, and the flat guess (a uniform circle) excites the first two radially symmetric modes. Figure 6 zooms in on four coefficients from the corner guess as they oscillate about zero. Recalling that lower mode numbers have the higher the eigenvalues, eigenmodes of higher number should be less correlated from cycle to cycle. This is shown in Fig. 6. Significant lag correlation is seen in the drift of mode 2, whereas mode 29 has a much tighter and uncorrelated oscillation about the value of zero. The lag-correlation coefficients were directly evaluated for these expansion coefficients, and some evidence of relation to the eigenvalue spectrum was found (as assumed in Ref. [6]). Lastly, for this problem, Fig. 8 shows the distribution of converged expansion coefficients, all of which indicate normality. The coefficients of mode 1 are not shown, as it is just converged by cycle 449. This shows how poor of an initial guess it is; strongly exciting the mode with the next-highest eigenvalue under mode 0 requires extensive neutron propagation

through generations to reach the fundamental.

The higher the mode number, the quicker it decays away as power iteration proceeds. As explained in the section 3.1, the power decay rate should be near  $K_n/K_0$ . Tables I and II compare the expected values versus the values found from doing a least squares fit of the coefficients before they die away. The agreement in Table I is quite bad, but better in Table II. This is most likely due to the larger batch size for later run (five times as large).

Table I. Empirical power decay rates of expansion coefficients for the center-point initial guess run (batch size = 1M), and relevant eigenvalue ratios.

Mode #	Cycle Range for Fit	Empirical Decay Rate	$K_i/K_0$	$C/E$
5	1-80	0.95371	0.95757	0.99597
10	1-30	0.90994	0.91655	0.99279
16	1-30	0.87385	0.87954	0.99354
25	1-15	0.80733	0.81315	0.99283
18	1-20	0.78111	0.78421	0.99605

Table II. Empirical power decay rates of expansion coefficients for the corner-point initial guess run (batch size = 500k), and relevant eigenvalue ratios.

Mode #	Cycle Range for Fit	Empirical Decay Rate	$K_i/K_0$	$C/E$
1	1-150	0.98609	0.98530	1.00080
3	1-100	0.96945	0.96756	1.00195
5	1-50	0.95810	0.95619	1.00199
7	1-50	0.94412	0.94058	1.00377
8	1-15	0.90134	0.92119	0.98822
9	1-20	0.89848	0.92118	0.97535
10	1-45	0.92062	0.91388	1.00737

### 4.3. Verification of fundamental adjoint weighting tallies

Figure 10 verifies the implementation of the spatial and energy-dependent adjoint weighting tallies in MCNP; plotted is the quantity  $\langle \Psi_0^\dagger, \Psi_0 \rangle_r / \langle \Psi_0 \rangle_r$ . The same problem is used in Ref. [4] to show increasing accuracy of adjoint weighting for increasing number of latent generations. The parameters for this 1-group problem are:  $\Sigma_t = 1.0 \text{ cm}^{-1}$ ,  $\Sigma_\gamma = 0.1 \text{ cm}^{-1}$ ,  $\Sigma_f = 0.2 \text{ cm}^{-1}$ ,  $\Sigma_{s0} = 0.7 \text{ cm}^{-1}$ , and  $\nu = 1.5$ . Since the problem is self-adjoint, the reference adjoint flux can be tallied directly. Figure 11 provides verification, with the discrete ordinates code PARTISN, for a 3-group problem, also used in Ref. [4].

#### 4.4 Test of kernel deflation

A problem was ran to examine the implementation of the kernel deflation process. Convergence to higher source modes, and subsequent stable oscillation about the expected shape, is verified. Issues could conceivably arise from an inadequate mesh size or from the effect of inflection points, but these problems are not seen here. A 3-group slab problem with vacuum boundaries is tested. The slab size is 40 cm; the other problem parameters are given in Table III. Before running this problem, a similar 1-group problem was found to have similar results as to those shown here.

Table III. Parameters for 3-Group Slab Problem

$g$	$\Sigma_t$	$\Sigma_f$	$\Sigma_\gamma$	$\chi$	$\Sigma_{s,g'1}$	$\Sigma_{s,g'2}$	$\Sigma_{s,g'3}$	$\bar{\nu}$
1	0.7	0	0.05	1	0.45	0.2	0	0
2	1.2	0	0.05	0	0	0.55	0.6	0
3	1.2	0.05	0.05	0	0	0	1.1	2.17

The source modes are calculated from a fission matrix tallied from 500 cycles of 100k histories. The mesh of these modes is  $100 \times 1 \times 1$ . Kernel deflation is then ran for modes 1-5, in addition to a run with the undeflated kernel; the initial distribution of all runs is flat and positive. 1000 cycles are ran, with a batch size of 10k. Viewing the cycle by cycle convergence of the different modes shows the different speed and manner in which each converge. These properties of convergence should be able to be predicted, just as in the case of an undeflated kernel. After convergence, reached by all modes by cycle 100, stable oscillation about the mean is seen, just as in active cycles of regular criticality calculations. Figure 12 shows mean and standard deviations of the fission bank distributions over cycles 100-1000. In the mean distribution plots, both the fission bank results and pre-computed fission matrix source modes (the expected values) are shown. The agreement between the two indicates the correctness and stability of the process. The relative standard deviations of the mean fission bank distributions are also shown; the values grow sharply near inflection points—especially in the case of mode #5.

#### 4.5 Test of higher-mode adjoint weighting

The same 40 cm slab problem of Table III is now used to evaluate the higher-mode adjoint weighting scheme. The same precomputed fission matrix is used—tallied for 500 cycles with a 100k batch size. Adjoint-weighting is then turned on; 3015 cycles with a batch size of 50k are ran with 20 latent generations. Energy and spatially-dependent adjoint-weighted flux is then tallied and plotted in Fig. 13. Note that, for actual perturbation and kinetics quantities, no energy or spatial binning is required, thus many less histo-

ries are needed for convergence of these quantities. Figure 13 shows there is an increasing bias for increasing mode number. The peaks are underestimated, and the critical points are overestimated.

A probable cause for the overestimation of the adjoint-weighted flux near critical points is the combination of the variation in sign of the tallies and the correlation of the the forward and adjoint tallies. If a positive forward flux is being tallied from a history in the original generation, it is most likely that the history will yield an asymptotic distribution that gives a positive adjoint flux. Similarly, a negative forward flux tally most likely leads to a negative adjoint tally. This positive correlation (or negative correlation, if the reference modes used for calculation adjoint flux are flipped) prevents the product of the tallies from converging to zero, as the product is almost always the same sign. Addressing this could possibly entail estimating a correlation coefficient, or somehow uncorrelating the two tallies.

## 5. CONCLUSIONS

This report has looked at ways in which higher-mode information of the fission matrix can be used to: better understand criticality calculations, and calculate new quantities of interest for practical design work. Decomposing the power iteration process into the behavior of the most important eigenmodes gives a clear picture of how neutrons propagate in space through generations, in addition to showing the effect of an initial guess on convergence. Next, it was shown for a typical 2D PWR problem that higher flux modes of reasonable statistical error could be calculated from fission source modes in a manageable amount of time.

Higher-mode adjoint weighting, a necessity for most practical applications of higher modes, motivated the look into fission kernel deflation. Kernel deflation aims to remove the effect of modes from the Green's function. This was first shown to have the effect on stable convergence to higher modes. It was also argued that this resulted in higher-mode adjoint weighting when the principle of iterated fission probability was applied. Results from a test problem gave good results in terms of overall shape and energy dependence, but an increasing bias was seen for increasing mode number. This bias is believed to be due to the effects of inflection points.

## 6. FUTURE WORK

The higher-mode adjoint weighting method used in Monte Carlo can be replicated with the 1D discrete ordinates written for this work. This could provide additional verification of the implementation in MCNP. The current issues are believed to be due to sampling and correlation—these issues would not be present with discrete ordinates. If

the current issues are fixed or ameliorated, harder problems will be tested involving: asymmetry, multiple spatial dimension, and continuous energy. This method is expected to fail for poor sampling and meshing—sampling and meshing requirements could be better understood. Calculating higher-mode perturbation and kinetics parameters will be key to understanding the usefulness of this work. This will entail examining their convergence properties and applying them to test problems. The perturbation theory discussed has been relevant to the calculation of the multiplication factor, but this could be extended to any response—such as heating in a region of space. Comparisons to existing higher-mode deterministic methods—from both diffusion theory discrete ordinates, will show the effect of Monte Carlo on the accuracy of these calculations.

An additional consideration is that for a realistic 3D problem, perturbation calculations may demand hundreds of modes. Calculating these from a fission matrix of some finite amount of tallies and mesh cells may be inadequate. Understanding the sensitivity of eigenmodes to mesh size and statistics, and possibly improving accuracy, is a possible future area of work.

#### Acknowledgments

This work was performed under an NEUP Fellowship received in 2012.

#### REFERENCES

1. F.B. BROWN, S.E. CARNEY, B.C. KIEDROWSKI, W.R. MARTIN “Fission Matrix Capability for MCNP, Part I - Theory”, *Proc. M&C 2013*, Sun Valley, ID, May 5-9 2013, on CD-ROM.
2. S.E. CARNEY, F.B. BROWN, B.C. KIEDROWSKI, W.R. MARTIN “Fission Matrix Capability for MCNP, Part II - Applications”, *Proc. M&C 2013*, Sun Valley, ID, May 5-9 2013, on CD-ROM.
3. J.T. Goorley, et. al., “Initial MCNP6 Release Overview—MCNP6 version 1.0,” LA-UR-13-22934, *Los Alamos National Laboratory* (2013).
4. B.C. KIEDROWSKI, F.B. Brown “Adjoint-Weighted Tallies for  $k$ -Eigenvalue Calculations with Continuous-Energy Monte Carlo”, *Nucl. Sci. Eng.*, **168**, pp 226-241 (2011).
5. B.E. TOTH, W.R. MARTIN, D.P. GRIESHEIMER, “Normality of Monte Carlo Criticality Eigenfunction Decomposition Coefficients”, *Proc. M&C 2013*, Sun Valley, ID, May 5-9 2013, on CD-ROM.
6. D.B. MACMILLAN, “Monte Carlo Confidence Limits for Iterated-Source Calculations”, *Nucl. Sci. Eng.*, **50**, pp 73-87 (1973).
7. S.E. CARNEY, F.B. BROWN, B.C. KIEDROWSKI, W.R. MARTIN “Fission Matrix Capability for MCNP Monte Carlo”, LA-UR-12-24533 (2012).
8. A. YAMAMOTO, K. SAKATA, T. ENDO, “Explicit Estimation of Higher Order Modes in Fission Source Distribution of Monte-Carlo Calculation”, *Proc. M&C 2013*, Sun Valley, ID, May 5-9 2013, on CD-ROM.
9. J.J. DUDERSTADT, L.J. HAMILTON, *Nuclear Reactor Analysis*, John Wiley & Sons (1976).
10. R.L. CHILDS, G.E. WHITESIDES, “Generalized Perturbation Theory using Two-Dimensional, Discrete Ordinates Transport Theory”, Oak Ridge National Lab, (1980).
11. K. HASHIMOTO, A. TATEMATSU, K. NISHINA, T. SHIBATA “Technical Notes: Interpretation of Control Rod Interaction Effect on the Basis of Modal Approach”, *Ann. Nucl. Energy*, **19**, pp 237-241 (1992).
12. R. MIRÓ, D. GINESTAR, G. VERDÚ, D. HENNIG “A Nodal Modal Method for the Neutron Diffusion Equation. Application to BWR Instabilities Analysis”, *Ann. Nucl. Energy*, **29**, pp 1171-1194 (2002).
13. S. GONZÁLEZ-PINTOR, D. GINESTAR, G. VERDÚ, “Time-Integration of the Neutron Diffusion Equation on Hexagonal Geometries”, *Math. & Comp. Modelling*, **52**, pp 1203-1210 (2010).
14. G.E. WHITESIDES, “A Difficulty in Computing the  $k$ -effective of the World”. *Trans ANS*, **14** [2], pp 680 (1971).

#### APPENDIX A

A modified Whitesides problem [14] was built and ran to examine the effects of a significantly asymmetric fission kernel. A  $5 \times 5$  PB-239 pin array with a 30 cm pitch is placed in water. Water acts as a reflector, 30 cm around the periphery. All pins except the center are 3.976 cm in radius; the center pin is 4.928 cm, and is covered in 1 cm of Cadmium. The Cadmium shell, a high-pass filter of neutrons, should result in a reduced amount of neutrons entering the center sphere to cause fission. Thus, the columns of the fission matrix in the vicinity of center mesh cells should be larger in magnitude than the respective rows, which is what Fig. 14 shows. Figs.15-19 gives eigenmode results for the first 30 modes. Table IV gives the spectrum calculated for the problem on a  $100 \times 100 \times 1$  mesh—surprisingly negligible imaginary components are found. This suggests that significantly-asymmetric fission matrices can still result in eigenmodes with minor imaginary components.

#### APPENDIX B

A 16-assembly BWR problem, with reflecting boundary conditions, was ran with both three and four control blades inserted. The first 30 fission source modes for both problems are shown in Figs. 20, 21. To understand the

Table IV. Eigenvalue spectrum for modified Whitesides problem. Fission matrix tallied with 200 cycles (2 initial skipped), 500k batch size;  $100 \times 100 \times 1$  mesh.

Mode #	Eigenvalue	Mode #	Eigenvalue
0	1.50991	15	1.32867
1	1.34361	16	1.32810
2	1.34257	17	1.32709
3	1.34228	18	1.32677
4	1.34036	19	1.32638
5	1.33844	20	1.32541
6	1.33667	21	1.32138
7	1.33605	22	1.31959
8	1.33457	23	1.31868
9	1.33360	24	1.31735
10	1.33337	25	$0.80960 + 2.85157 \times 10^{-4}i$
11	1.33217	26	$0.80960 - 2.85157 \times 10^{-4}i$
12	1.33134	27	0.67165
13	1.33051	28	0.67121
14	1.32909	29	0.67079

requirements for perturbation calculations, the fundamental mode of the 4-blade problem is expanded in terms of higher modes from the 3-blade problem. Fig. 22 shows the relative errors from this expansion for an increasing number of modes. Fig. 23 gives the values of the expansion coefficients and relative error stats. While the perturbation of the control rod insertion is represented well with the expansion throughout most of the problem, in the vicinity of the insertion the relative error cannot get better than about 400%. For increasing degree of expansion, the error is not monotonically decreasing—expansion modes can introduce errors which further expansion modes reduce.

## FIGURES

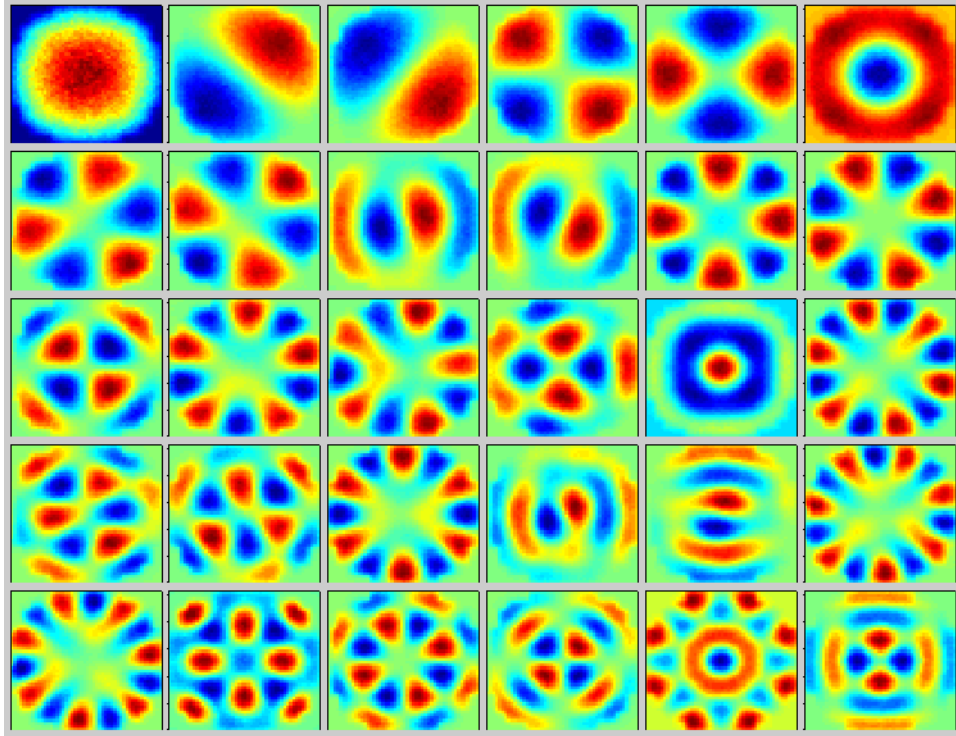


Fig. 1. First 30 forward flux modes of 2D PWR, group 1 (0.625 eV to 20 MeV). Fission matrix tallied with 500 cycles, 500k batch size;  $50 \times 50 \times 1$  mesh; 500k histories for each fixed-source calculation.

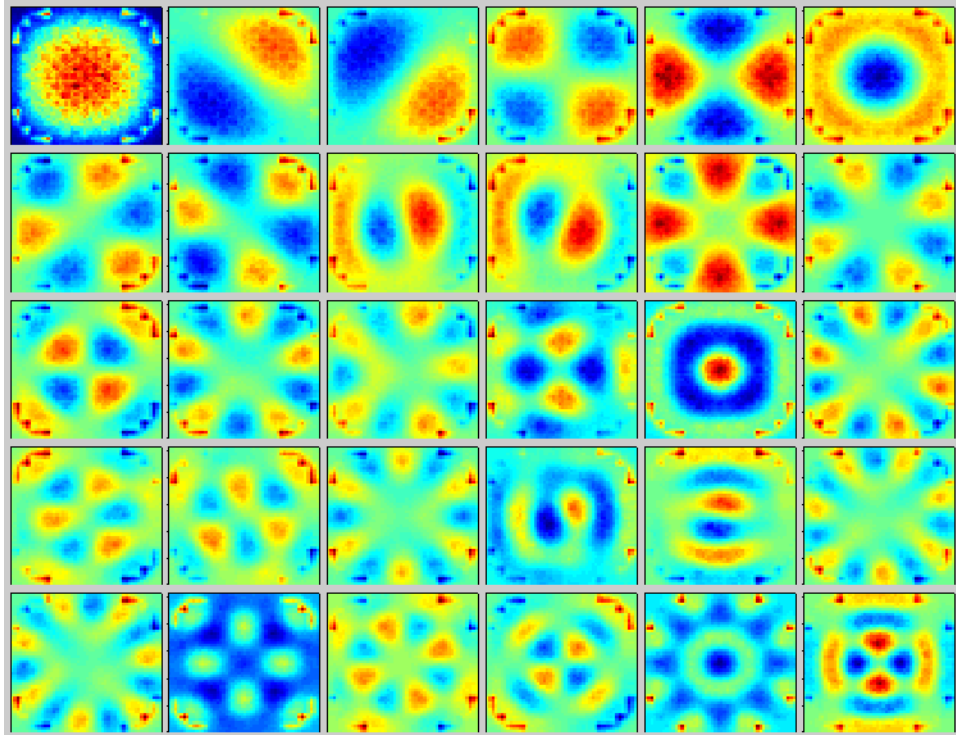


Fig. 2. First 30 forward flux modes of 2D PWR, group 2 (0 to 0.625 eV). Fission matrix tallied with 500 cycles, 500k batch size;  $50 \times 50 \times 1$  mesh; 500k histories for each fixed-source calculation.

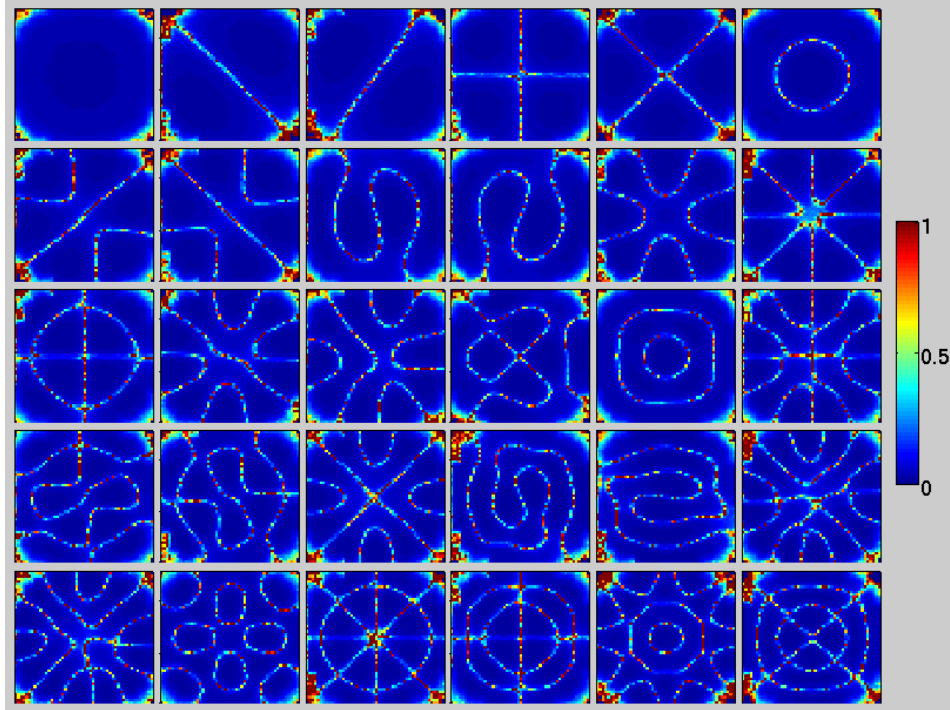


Fig. 3. Relative uncertainty of first 30 forward flux modes of 2D PWR, group 1 (0.625 eV to 20 MeV). Fission matrix tallied with 500 cycles, 500k batch size;  $50 \times 50 \times 1$  mesh; 500k histories for each fixed-source calculation.

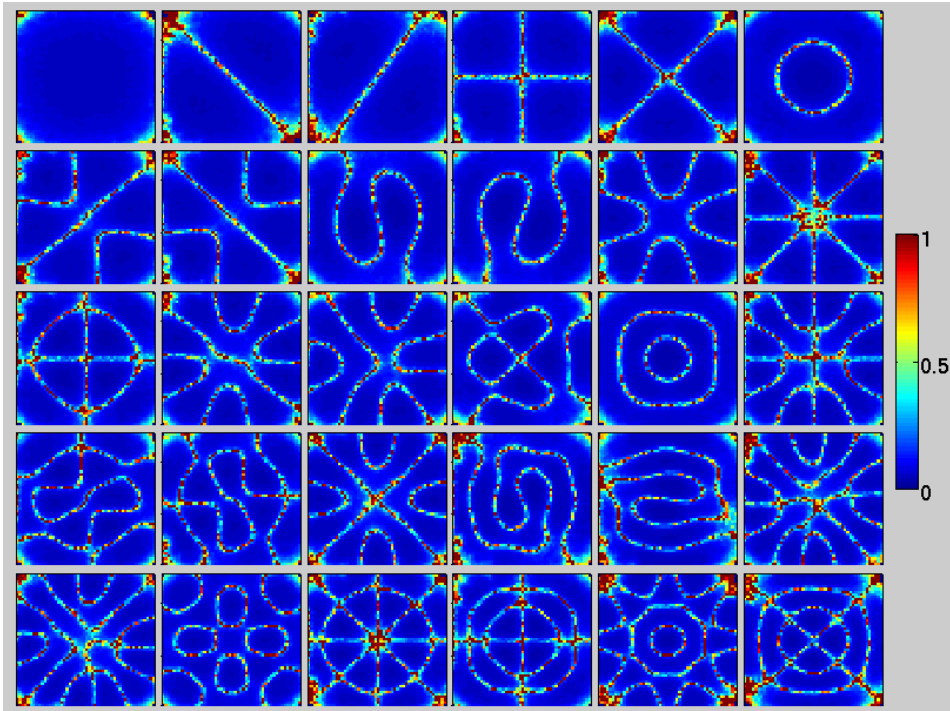


Fig. 4. Relative uncertainty of first 30 forward flux modes of 2D PWR, group 2 (0 to 0.625 eV). Fission matrix tallied with 500 cycles, 500k batch size;  $50 \times 50 \times 1$  mesh; 500k histories for each fixed-source calculation.

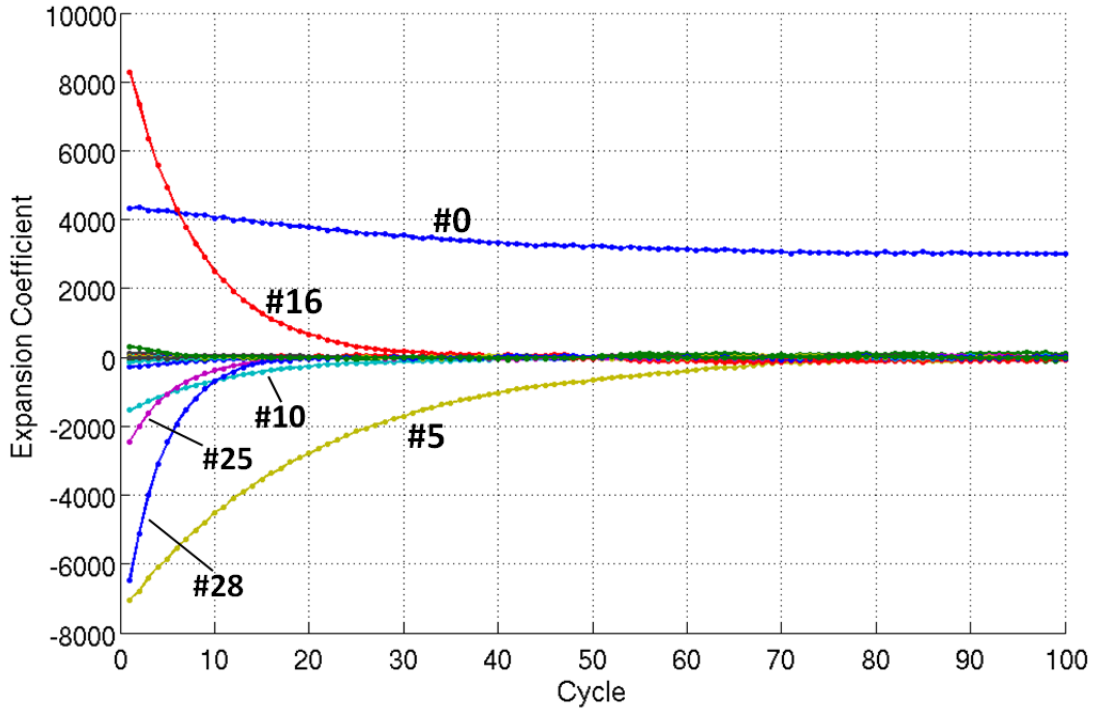


Fig. 5. First 30 eigenmode expansion coefficients for 2D PWR problem; initial guess is the center point. Fission matrix tallied with 500 cycles, 500k batch size;  $50 \times 50 \times 1$  mesh; 100 cycles and 100k batch size for coefficient calculation.

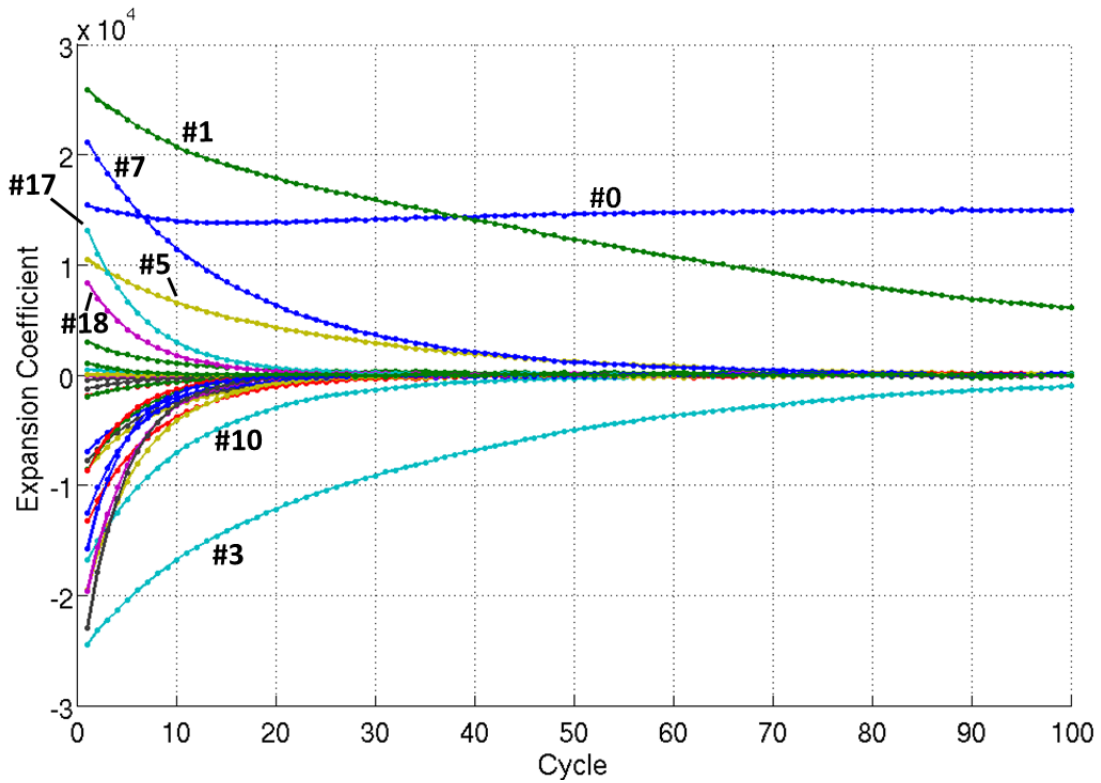


Fig. 6. First 30 eigenmode expansion coefficients for 2D PWR problem; initial guess is a point in the corner. Fission matrix tallied with 500 cycles, 500k batch size;  $50 \times 50 \times 1$  mesh; 449 cycles and 500k batch size for coefficient calculation.

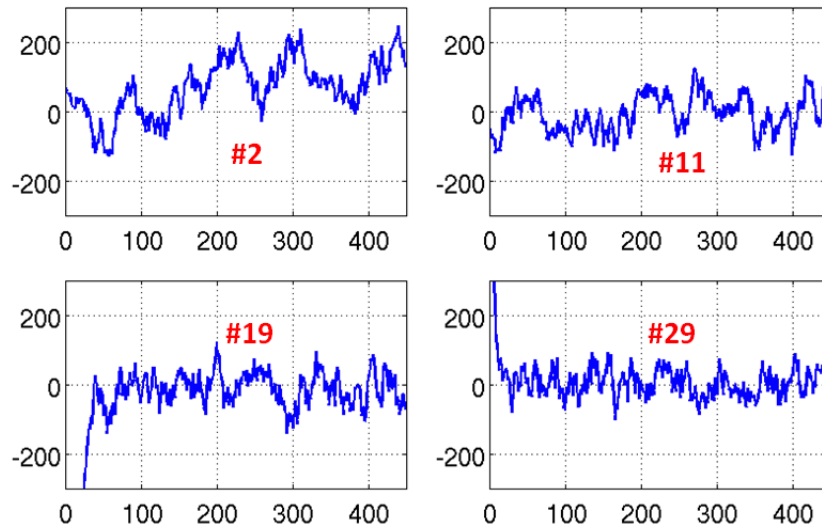


Fig. 7. Eigenmode expansion coefficients #2,11,19,29 for 2D PWR problem; initial guess is a point in the corner. Fission matrix tallied with 500 cycles, 500k batch size;  $50 \times 50 \times 1$  mesh; 449 cycles and 500k batch size for coefficient calculation.

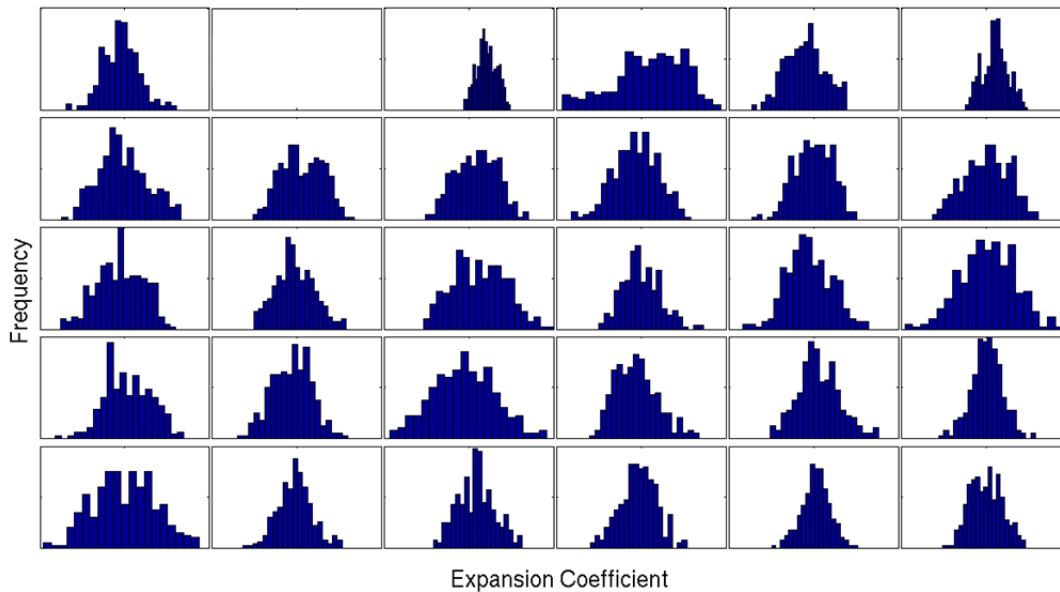


Fig. 8. Distribution of eigenmode expansion coefficients for 2D PWR problem; initial guess is a point in the corner. Cycle 150-449 coefficients used for all except #1unconverged and #3cycles 200-449. Fission matrix tallied with 500 cycles, 500k batch size;  $50 \times 50 \times 1$  mesh; 449 cycles and 500k batch size for coefficient calculation.

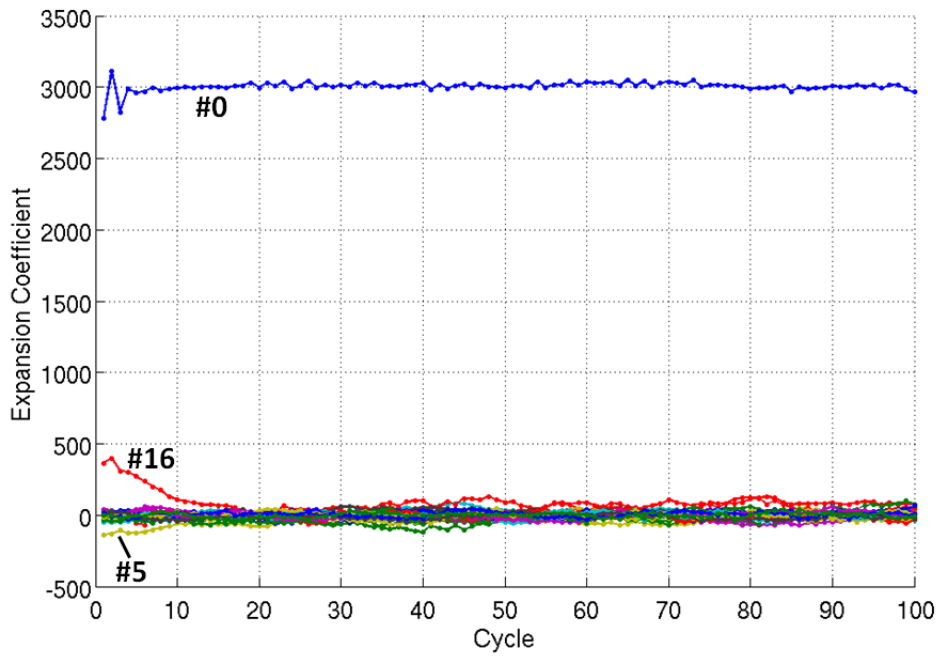


Fig. 9. First 30 eigenmode expansion coefficients for 2D PWR problem; initial guess is a uniform throughout problem. Fission matrix tallied with 500 cycles, 500k batch size;  $50 \times 50 \times 1$  mesh; 100 cycles and 500k batch size for coefficient calculation.

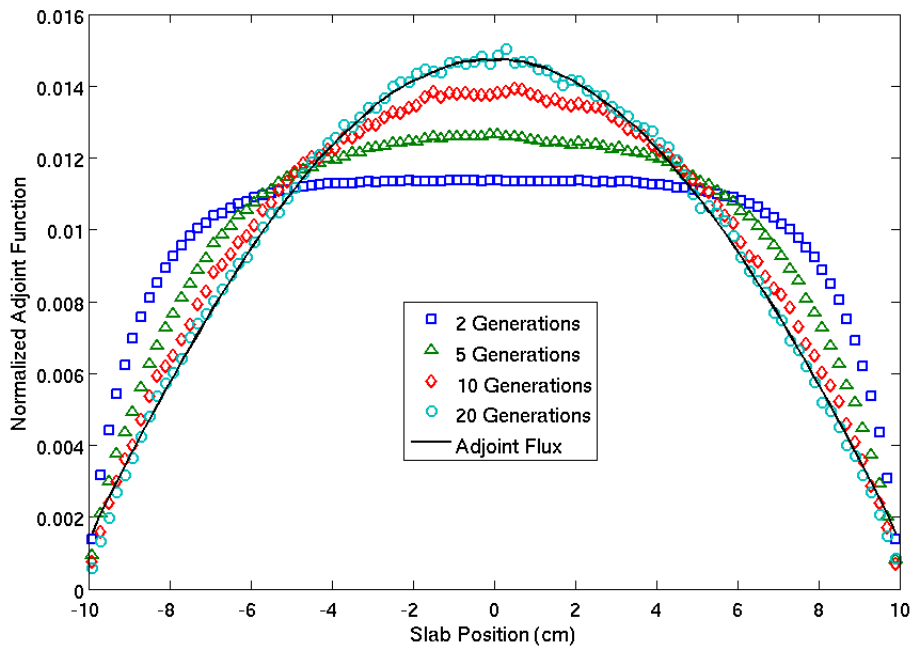


Fig. 10. Adjoint flux approximations for a 1D, 1-group problem, with a varying number of latent generations

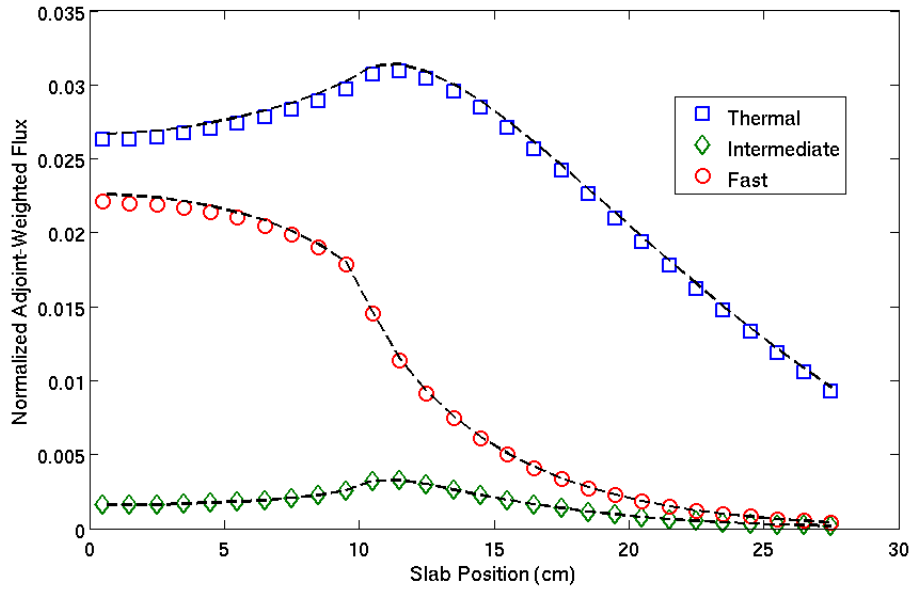


Fig. 11. Adjoint-weighted fluxes for two-region, 3-group problem, calculated with PARTISN and MCNP

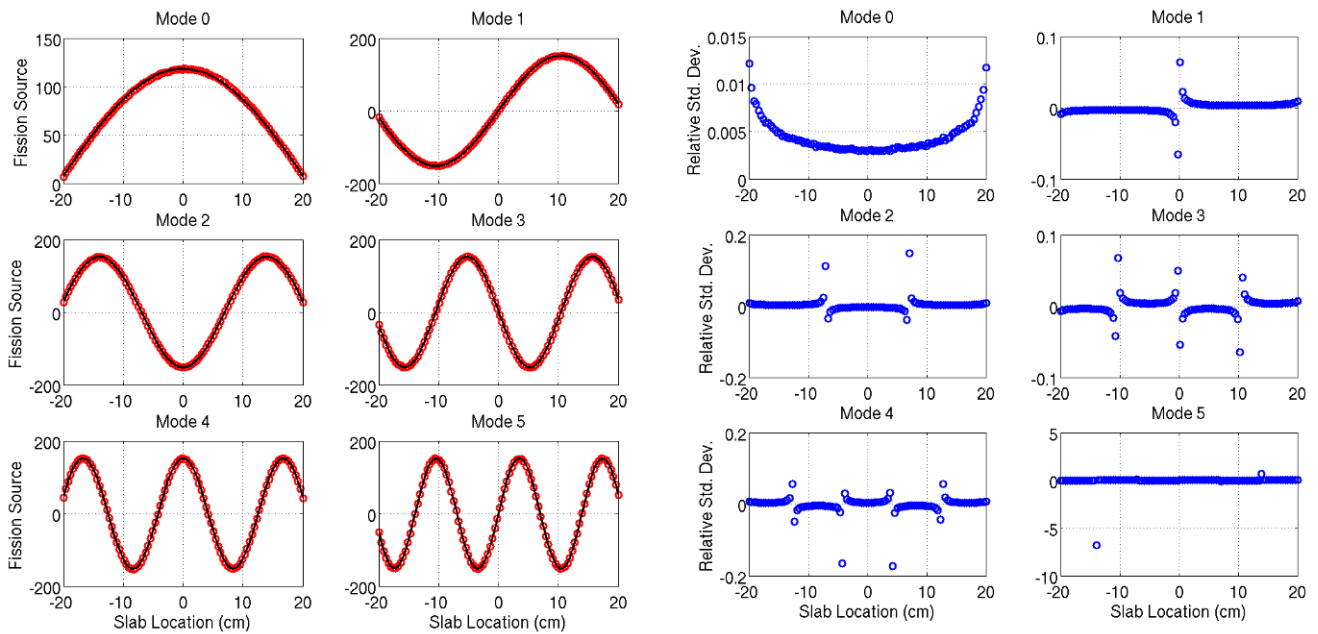


Fig. 12. Mean & relative standard deviation of fission bank distribution for cycles 100-1000. Fission matrix source modes, the expected values, are also plotted with the means.

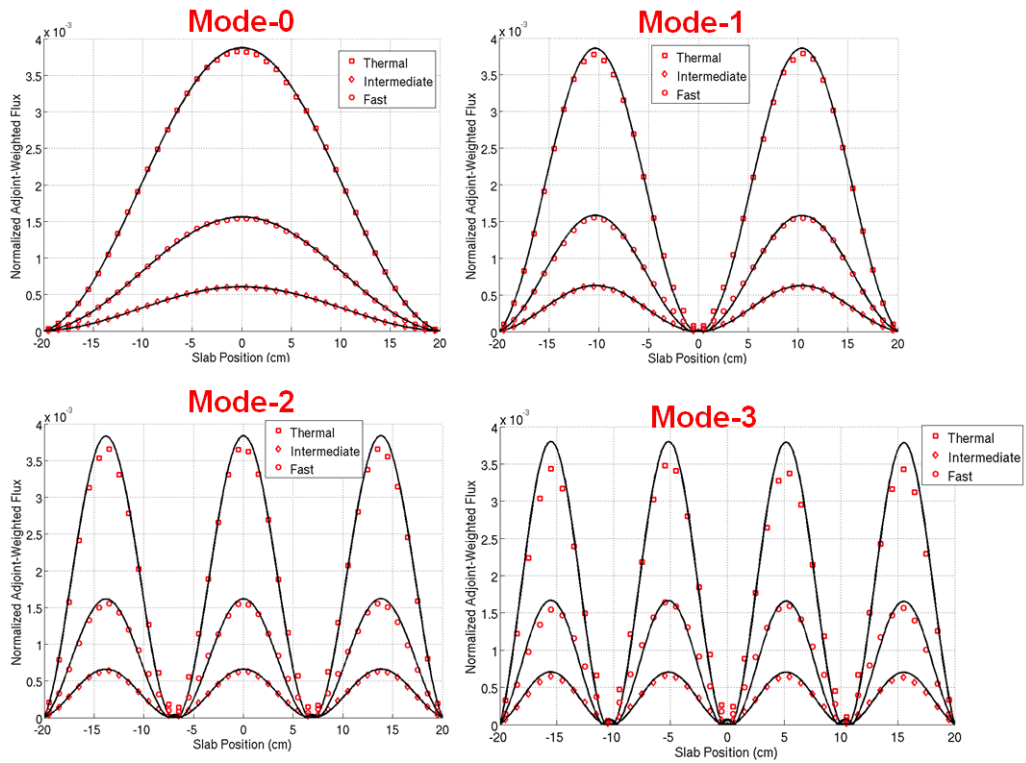


Fig. 13. Normalized, 3-group adjoint-weighted flux of modes 0-4. Monte Carlo and  $S_{16}$  results plotted.

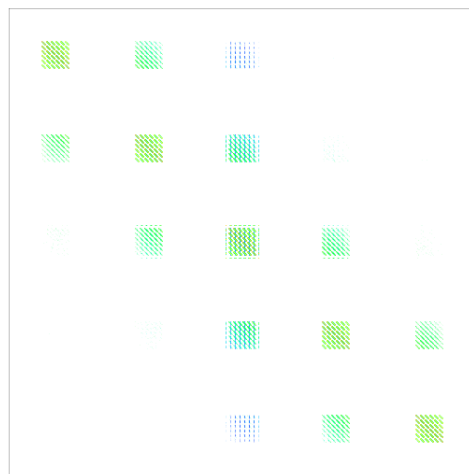


Fig. 14. Fission matrix structure of modified Whitesides problem. Fission matrix tallied with 200 cycles (2 initial skipped), 500k batch size;  $100 \times 100 \times 1$  mesh.

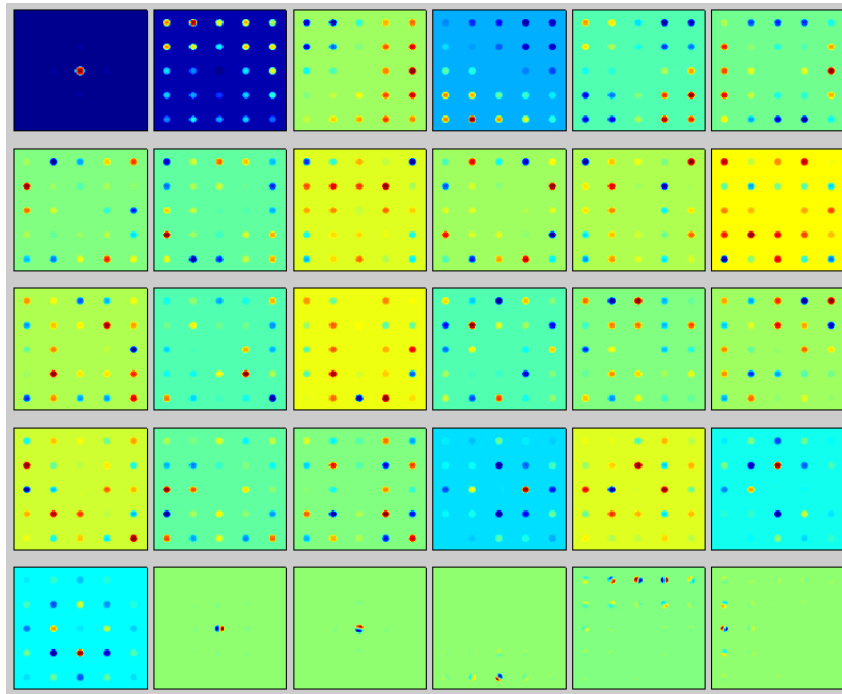


Fig. 15. Forward fission source modes of modified Whitesides problem. Fission matrix tallied with 200 cycles (2 initial skipped), 500k batch size;  $100 \times 100 \times 1$  mesh.

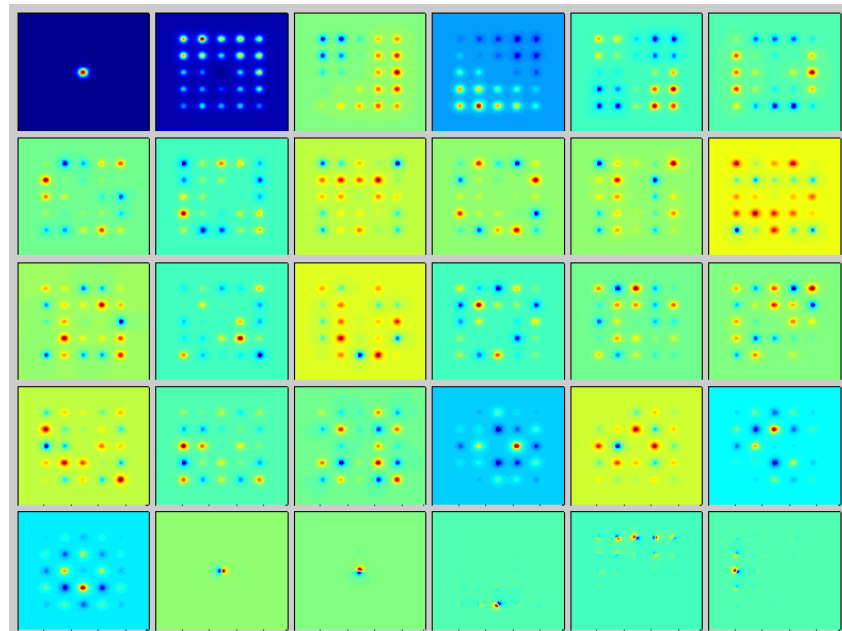


Fig. 16. Forward flux modes of modified Whitesides problem, group 1 (0.625 eV to 20 MeV). Fission matrix tallied with 200 cycles (2 initial skipped), 500k batch size;  $100 \times 100 \times 1$  mesh; 1M histories for fixed-source calculations, tallied on a  $240 \times 240 \times 1$  mesh

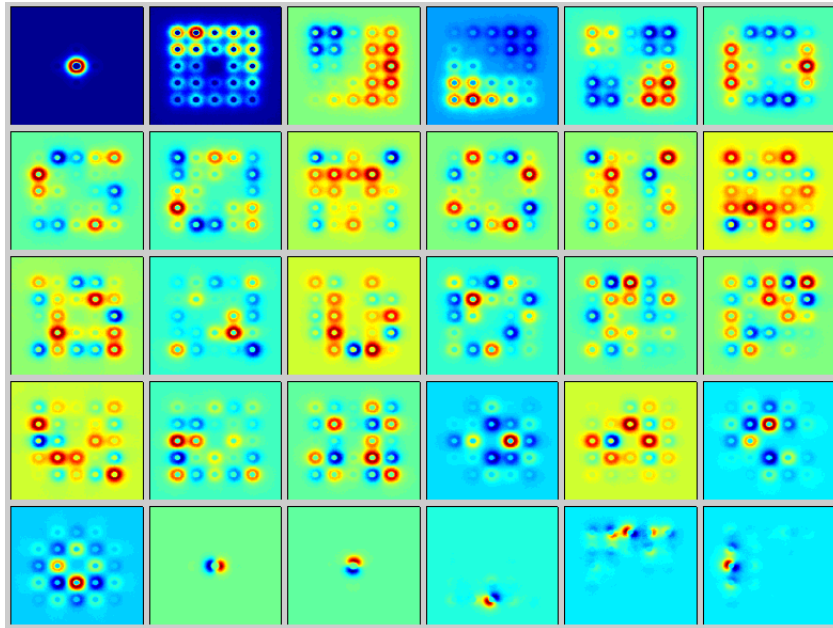


Fig. 17. Forward flux modes of modified Whitesides problem, group 2 (0 to 0.625 eV). Fission matrix tallied with 200 cycles (2 initial skipped), 500k batch size;  $100 \times 100 \times 1$  mesh; 1M histories for fixed-source calculations, tallied on a  $240 \times 240 \times 1$  mesh

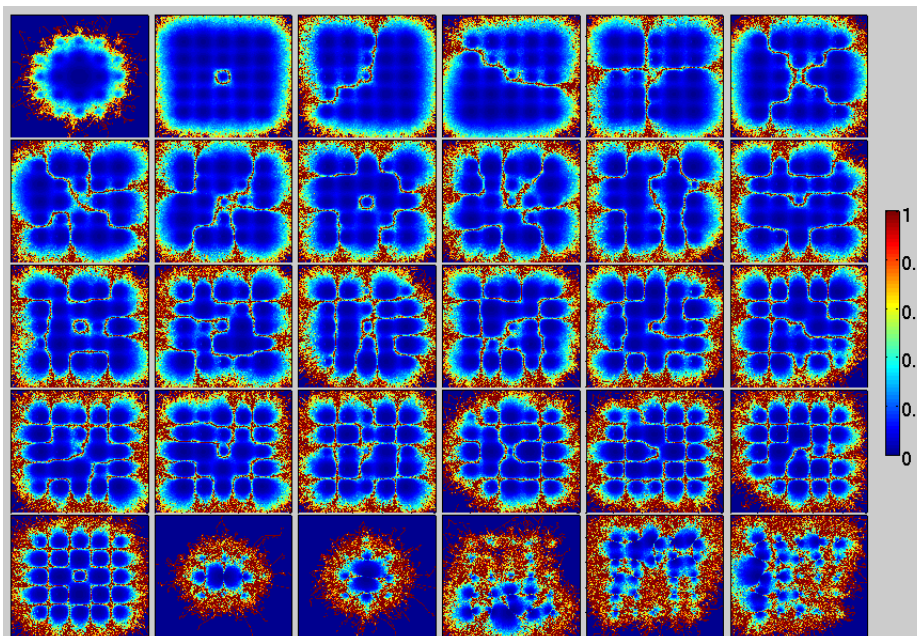


Fig. 18. Relative uncertainty of forward flux modes for modified Whitesides problem, group 1 (0.625 eV to 20 MeV). Fission matrix tallied with 200 cycles (2 initial skipped), 500k batch size;  $100 \times 100 \times 1$  mesh; 1M histories for fixed-source calculations, tallied on a  $240 \times 240 \times 1$  mesh

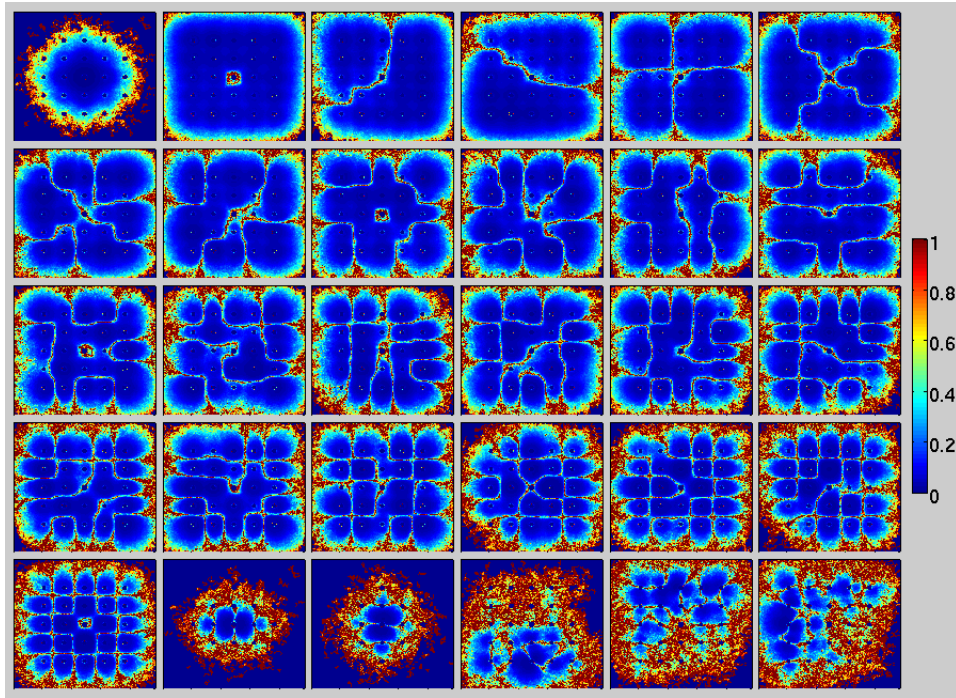


Fig. 19. Relative uncertainty of forward flux modes for modified Whitesides problem, group 2 (0 to 0.625 eV). Fission matrix tallied with 200 cycles (2 initial skipped), 500k batch size;  $100 \times 100 \times 1$  mesh; 1M histories for fixed-source calculations, tallied on a  $240 \times 240 \times 1$  mesh

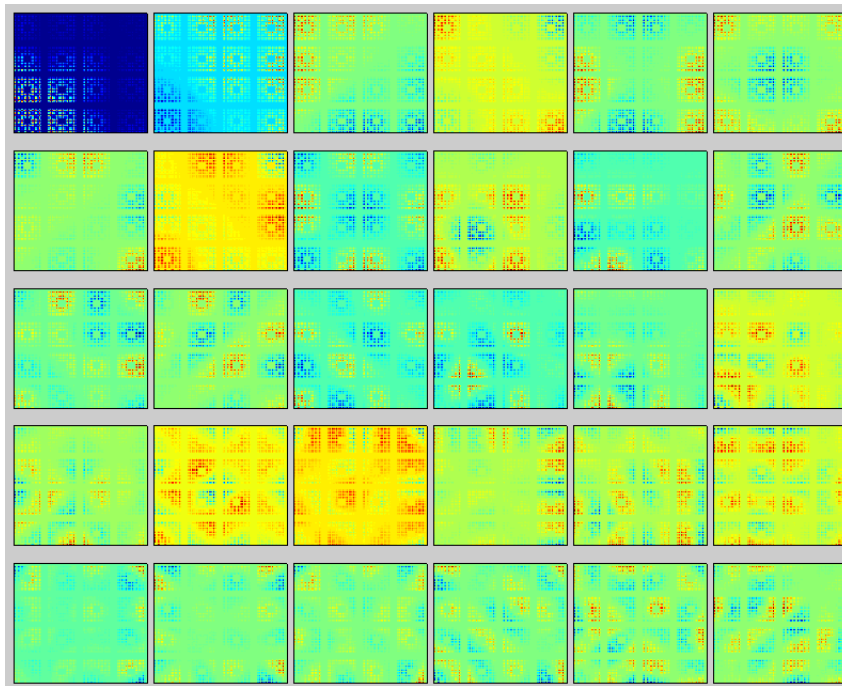


Fig. 20. Forward fission source modes for 16-assembly BWR problem with reflecting boundary conditions and 3 control blades inserted.  $100 \times 100 \times 1$  mesh.

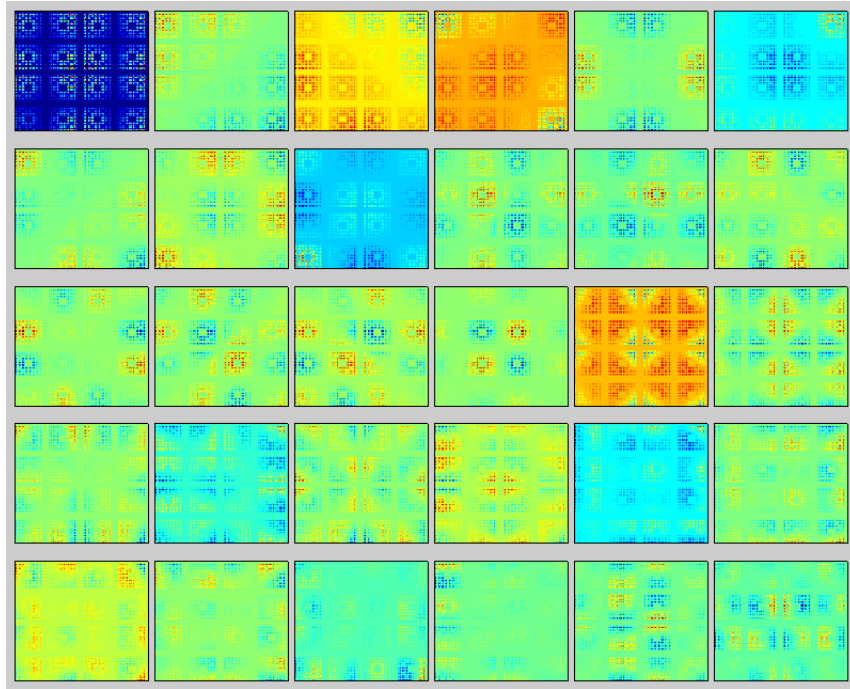


Fig. 21. Forward fission source modes for 16-assembly BWR problem with reflecting boundary conditions and 4 control blades inserted.  $100 \times 100 \times 1$  mesh.

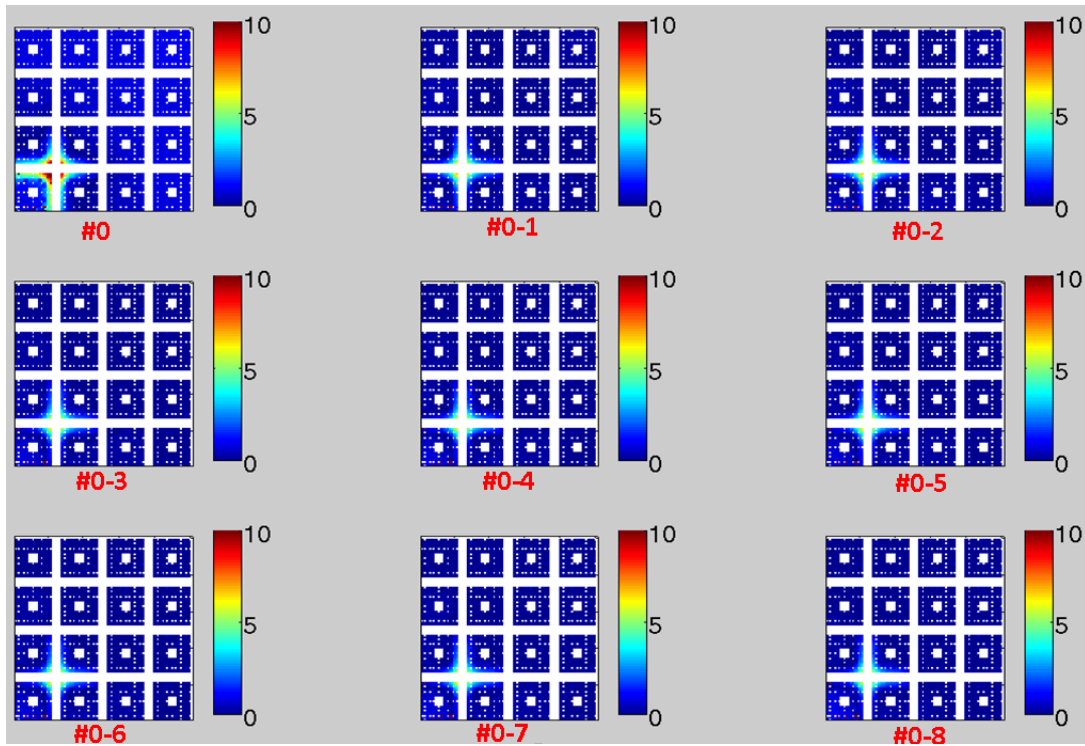


Fig. 22. Relative error of 4-control blade problem fundamental mode representation with increasing number of eigenmodes from 3-control blade problem.

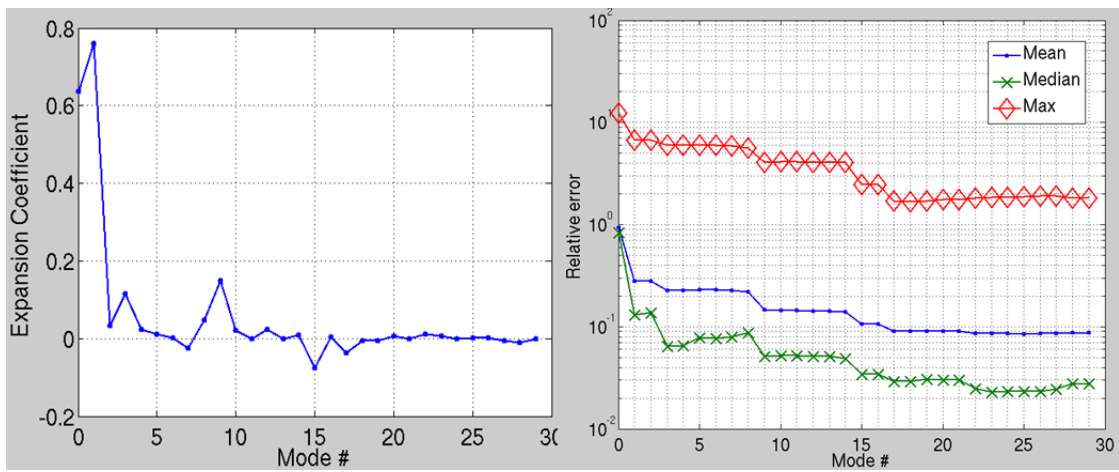


Fig. 23. Expansion coefficients and error stats of 3-control blade problem eigenmodes expansion to 4-control blades problem fundamental.